Geophysical Journal International

Geophys. J. Int. (2011) **184,** 507–526 doi: 10.1111/j.1365-246X.2010.04859.x

3-D frequency-domain seismic wave modelling in heterogeneous, anisotropic media using a Gaussian quadrature grid approach

Bing Zhou[1] and S. A. Greenhalgh[1,2]

[1] *Department of Physics, The University of Adelaide, SA* 5005, *Australia. E-mail: bing.zhou@adelaide.edu.au*
[2] *Institute of Geophysics, ETH Zürich,* 8092 *Zürich, Switzerland*

Accepted 2010 October 18. Received 2010 August 2; in original form 2010 January 8

SUMMARY

We present an extension of the 3-D spectral element method (SEM), called the Gaussian quadrature grid (GQG) approach, to simulate in the frequency-domain seismic waves in 3-D heterogeneous anisotropic media involving a complex free-surface topography and/or sub-surface geometry. It differs from the conventional SEM in two ways. The first is the replacement of the hexahedral element mesh with 3-D Gaussian quadrature abscissae to directly sample the physical properties or model parameters. This gives a point-gridded model which more exactly and easily matches the free-surface topography and/or any sub-surface interfaces. It does not require that the topography be highly smooth, a condition required in the curved finite difference method and the spectral method. The second is the derivation of a complex-valued elastic tensor expression for the perfectly matched layer (PML) model parameters for a general anisotropic medium, whose imaginary parts are determined by the PML formulation rather than having to choose a specific class of viscoelastic material. Furthermore, the new formulation is much simpler than the time-domain-oriented PML implementation. The specified imaginary parts of the density and elastic moduli are valid for arbitrary anisotropic media. We give two numerical solutions in full-space homogeneous, isotropic and anisotropic media, respectively, and compare them with the analytical solutions, as well as show the excellent effectiveness of the PML model parameters. In addition, we perform numerical simulations for 3-D seismic waves in a heterogeneous, anisotropic model incorporating a free-surface ridge topography and validate the results against the 2.5-D modelling solution, and demonstrate the capability of the approach to handle realistic situations.

Key words: Numerical solutions; Body waves; Seismic anisotropy; Seismic tomography; Computational seismology; Wave propagation.

INTRODUCTION

Seismic diffraction tomography (Wu & Toksoz 1987; Gelius 1995) and frequency-domain full-waveform inversion (Pratt 1999; Greenhalgh & Zhou 2003; Zhou & Greenhalgh 2003; Ali *et al*. 2008) are two separate but closely related high-resolution seismic imaging techniques, which have great potential in hydrocarbon exploration and investigations of the Earth's interior. The most attractive aspect of these two techniques is the capability to obtain sub-wavelength resolution images of the sub-surface from the observed seismogram spectra at just a few frequencies, thus significantly reducing the computational demands of the imaging process (Gelius 1995; Pratt 1999; Maurer *et al*. 2009). To implement such imaging methods, one either performs frequency-domain seismic wave forward modelling that involves application of an appropriate numerical method to solve the frequency-domain wave equation for a given earth model, specified source–receiver configuration and range of frequencies, or efficiently extracts the frequency wavefield from a time-domain modelling tool (Nihei & Xiaoye 2007; Sirgue *et al*. 2008). The frequency-domain forward modelling yields the synthetic seismogram spectral data, that is, the real and imaginary parts of the seismogram spectra, or the amplitude and phase spectra. In an inversion, this information is matched with the observed spectral data by successively upgrading the earth model. Recently, Fichtner *et al*. (2009a) and Tape *et al*. (2009) demonstrated great progress in time-domain full waveform inversion.

Mathematically, the traditional numerical solvers, such as finite difference and finite element methods (Kelley & Marfurt 1990; Dumbser *et al*. 2007; Basabe *et al*. 2008), and some modern approaches, such as the spectral method (Kosloff *et al*. 1990; Tessmer 1995; Furumura *et al*. 1998; Trefethen 2000) and the spectral element method (SEM) (Faccioli *et al*. 1997; Komatitsch & Vilotte 1998; Komatitsch & Tromp 2002; Sinclair *et al*. 2007; Emanuele *et al*. 2007; Fichtner *et al*. 2009b), are all applicable to frequency-domain seismic wave modelling. Each

of the solvers has its own advantages and limitations. For example, the traditional finite difference method is simple in implementation, but cannot be easily extended to geological models having a complex geometry, like free-surface topography or irregular subsurface interfaces. The spectral method is a highly accurate method and valid for a complex geometry (Tessmer 1995; Igel 1999), but it gives a fully filled-in system matrix that may cost a huge amount of computer memory and run time in 3-D modelling. The finite element method and the SEM are in principle capable of handling arbitrary earth models having a complex geometry, for which a powerful element mesh generator, such as the Delaunay Triangulator (2-D) (Shewchuk 2002) or TetGen (3-D) (Rücker *et al.* 2006; Kerry & Weiss 2006) is often applied to create an element mesh which fits the complex free-surface and sub-surface geometry. For simplicity, most users of 3-D spectral element modelling employ a hexahedral element mesh that offers two advantages: implementation of the simple model parametrization (i.e. constant element-meshed model) and easy distribution of the Guassian-Lobatto-Legendre abscissae for the elemental integration. However, such a hexahedral element mesh is less competitive in matching the complex topography of the free-surface or the sub-surface interfaces than an unstructured tetrahedral element mesh (Rücker *et al.* 2006). However, when employing such an unstructured tetrahedral element mesh generator, one hardly knows in advance the mesh node locations in the forward modelling or inversion. To make the numerical modelling valid for complex free-surface topography, Carcione (1994) suggested solving the wave equations in a generalized coordinate system, whereas Komatitsch *et al*. (1996) demonstrated a non-linear transform of the Cartesian coordinate system into a specified curved coordinate system in terms of the free-surface and sub-surface interface geometry. Hestholm & Ruud (1998) presented another transform that converts a curved grid into a rectangular grid in 3-D using the finite difference method, and showed the peculiar features of wave propagation beneath a hill and valley topography. However, all three methods apply different global curved coordinate transforms to the governing wave equation so that they are limited by the shape of the topographic surfaces, which must be high-order differentiable or smooth enough for the transforms to be taken.

Recently, we developed a revised version of the SEM, called the 'Gaussian Quadrature Grid' (GQG) approach, for geophysical modelling problems. We have successfully applied it to 2.5-D and 3-D geoelectrical resistivity modelling (Zhou *et al.* 2009). The GQG approach differs from the common SEM in the two aspects. First, we replace the hexahedral element mesh with a point-gridded mesh formed by Gaussian quadrature abscissa that combines the definition of the physical properties of the model and the computation of the weak form of intergral solution. The GQG actually simplifies the model discretization and becomes more competitive in matching the 3-D free-surface or sub-surface topographic surfaces than the hexahedral element mesh in the common SEM, as well as providing easier control of the model parametrization than an unstructured tetrahedral element mesh for the inversion. Second, the GQG approach is an extension of the time-domain SEM to frequency-domain seismic wave modelling, for which we developed a new implementation of perfectly matched layers (PML) to remove the artificial reflections from the computational domain boundaries. We demonstrate that suppressing the grid margin reflections can be simply accomplished using the so-called 'PML model parameters' (density and elastic moduli), whose imaginary parts are specified in terms of the PML formulation and are valid for arbitrary anisotropic media. Therefore, the most attractive features of the GQG approach are simplification of the model discretization, easy implementation of the PMLs for heterogeneous, anisotropic media and the capability for handling complex model geometry.

In this paper, we extend the GQG approach to 3-D frequency-domain seismic wave modelling in general anisotropic media, which covers as special cases isotropic, vertical transversely isotropic (VTI) and tilted transversely isotropic (TTI) media. The latter two classes of anisotropy are often encountered in seismic exploration (Thomsen 1986) and earthquake seismology/deep seismic sounding (Crampin 1981), where layering, foliation and rock fracturing are present. Our aim is to utilize the GQG approach as a powerful tool for 3-D non-linear seismic diffraction tomography and frequency-domain full-waveform inversion with seismogram spectral data. The remaining parts of this paper are organized into four sections: the first section briefly gives the 3-D wave equation that incorporates a new implementation of the PML; the second section describes the numerical implementation of the 3-D frequency-domain GQG approach, while in the third section we give three numerical examples that show the accuracies and capabilities of the GQG approach for simulating seismic waves in isotropic and heterogeneous, anisotropic media. In the last section we draw some conclusions from this research.

BASIC EQUATIONS

The 3-D elastodynamic wave equation in the frequency-domain is given by (Aki & Richards 1980).

$$\frac{\partial}{\partial x_i}\left(c_{ijkl}\frac{\partial u_k}{\partial x_l}\right)+\rho\omega^2 u_j+f_j(\omega)\delta(\mathbf{r}-\mathbf{r}_s)=0,\qquad \mathbf{r},\mathbf{r}_s\in\Omega, \tag{1}$$

where u_j is the Fourier transformed displacement vector, $\delta(\mathbf{r})$ is Dirac delta, c_{ijkl} is the fourth-rank elastic modulus tensor that may involve complex values in viscoelastic media (Carcione 2001), ρ is the density of the medium and $f_j(\omega)$ is the point source force vector located at position $\mathbf{r}_s=(x_s, y_s, z_s)$ and acting in coordinate direction j, having specified spectrum $f(\omega)$. Repetition of subscripts in eq. (1) implies summation over all values $i, k, l\ (=x, y, z)$.

As a physical principle, to both prevent and absorb any artificial reflections from the model boundaries due to the limited computational domain Ω in numerical modelling, one may simply incorporate a viscoelastic (damping) medium in the margin areas. The viscoelastic material is defined by complex-valued moduli $\tilde{c}_{ijkl}=\mathrm{Re}(\tilde{c}_{ijkl})+\mathrm{i}\ \mathrm{Im}(\tilde{c}_{ijkl})$. The imaginary part $\mathrm{Im}(\tilde{c}_{ijkl})$ is not unique and depends on the choice of the viscoelastic material used (Carcione 2001). Here, we apply a simple PML definition to obtain the analytic expressions of the

complex-valued moduli. According to the PML principle, we define the complex coordinates as follows:

$$\tilde{x} = x - \mathrm{i}\int_0^x b(\xi)\,\mathrm{d}\xi, \tag{2}$$

to the boundary having its normal in the x-direction, that is, the PML is on the right and left margins having their normals in the x-direction. Here, the stretched coordinate part is frequency independent and differs from the original definition (Berenger 1994). We used such a simple form to obtain a frequency-independent tensor $\tilde{c}_{ijkl}$ that effectively achieves the wave damping within the finite thickness layer that is placed around the borders of the model edges. Obviously, if $b(\xi) = 0$, we have $\tilde{x} = x$. The derivative for the general case is:

$$\frac{\partial \tilde{x}}{\partial x} = 1 - \mathrm{i}b(x). \tag{3}$$

The wave equation (eq. 1) incorporating the PML takes on the following form, simply by changing the real coordinate x into the complex coordinate $\tilde{x}$:

$$\frac{\partial}{\partial \tilde{x}}\left(c_{1jk1}\frac{\partial u_k}{\partial \tilde{x}} + c_{1jk2}\frac{\partial u_k}{\partial y} + c_{1jk3}\frac{\partial u_k}{\partial z}\right) + \frac{\partial}{\partial y}\left(c_{2jk1}\frac{\partial u_k}{\partial \tilde{x}} + c_{2jk2}\frac{\partial u_k}{\partial y} + c_{2jk3}\frac{\partial u_k}{\partial z}\right)$$
$$+ \frac{\partial}{\partial z}\left(c_{3jk1}\frac{\partial u_k}{\partial \tilde{x}} + c_{3jk2}\frac{\partial u_k}{\partial y} + c_{3jk3}\frac{\partial u_k}{\partial z}\right) + \rho\omega^2 u_j = 0. \tag{4}$$

Here, the source term is omitted because the PMLs are far removed from the point-source position. Applying the differential chain rule

$$\frac{\partial u_k}{\partial \tilde{x}} = \frac{\partial u_k}{\partial x}\frac{\partial x}{\partial \tilde{x}} = \frac{1}{1 - \mathrm{i}b(x)}\frac{\partial u_k}{\partial x}, \tag{5}$$

we rewrite eq. (4) as follows:

$$\frac{1}{1-\mathrm{i}b(x)}\frac{\partial}{\partial x}\left[\frac{c_{1jk1}}{1-\mathrm{i}b(x)}\frac{\partial u_k}{\partial x} + c_{1jk2}\frac{\partial u_k}{\partial y} + c_{1jk3}\frac{\partial u_k}{\partial z}\right] + \frac{\partial}{\partial y}\left[\frac{c_{2jk1}}{1-\mathrm{i}b(x)}\frac{\partial u_k}{\partial x} + c_{2jk2}\frac{\partial u_k}{\partial y} + c_{2jk3}\frac{\partial u_k}{\partial z}\right]$$
$$+ \frac{\partial}{\partial z}\left[\frac{c_{3jk1}}{1-\mathrm{i}b(x)}\frac{\partial u_k}{\partial x} + c_{3jk2}\frac{\partial u_k}{\partial y} + c_{3jk3}\frac{\partial u_k}{\partial z}\right] + \rho\omega^2 u_j = 0. \tag{6}$$

Multiplying $[1 - \mathrm{i}b(x)]$ to both sides of the above equation, we obtain

$$\frac{\partial}{\partial x}\left(\tilde{c}_{1jk1}\frac{\partial u_k}{\partial x} + c_{1jk2}\frac{\partial u_k}{\partial y} + c_{1jk3}\frac{\partial u_k}{\partial z}\right) + \frac{\partial}{\partial y}\left(c_{2jk1}\frac{\partial u_k}{\partial x} + \tilde{c}_{2jk2}\frac{\partial u_k}{\partial y} + \tilde{c}_{2jk3}\frac{\partial u_k}{\partial z}\right) + \frac{\partial}{\partial z}\left(c_{3jk1}\frac{\partial u_k}{\partial x} + \tilde{c}_{3jk2}\frac{\partial u_k}{\partial y} + \tilde{c}_{3jk3}\frac{\partial u_k}{\partial z}\right) + \tilde{\rho}^{(1)}\omega^2 u_j$$
$$= \frac{\partial}{\partial x_i}\left(\tilde{c}^{(1)}_{ijkl}\frac{\partial u_k}{\partial x_l}\right) + \tilde{\rho}^{(1)}\omega^2 u_j = 0, \tag{7}$$

where the density and the elastic moduli are defined in the following way:

$$\tilde{\rho}^{(1)} = [1 - \mathrm{i}b(x)]\rho,$$
$$\tilde{c}^{(1)}_{ijkl} = \begin{bmatrix} \dfrac{c_{1jk1}}{[1-\mathrm{i}b(x)]} & c_{1jk2} & c_{1jk3} \\ c_{2jk1} & [1-\mathrm{i}b(x)]c_{2jk2} & [1-\mathrm{i}b(x)]c_{2jk3} \\ c_{3jk1} & [1-\mathrm{i}b(x)]c_{3jk2} & [1-\mathrm{i}b(x)]c_{3jk3} \end{bmatrix}. \tag{8}$$

In a similar manner, we obtain the following equations incorporating the PMLs having their normals in the y-($n = 2$) and z-($n = 3$) directions (i.e. the y-PML refers to the back and front of the model, whereas the z-PML refers to the bottom of the model).

$$\frac{\partial}{\partial x_i}\left(\tilde{c}^{(n)}_{ijkl}\frac{\partial u_k}{\partial x_l}\right) + \tilde{\rho}^{(n)}\omega^2 u_j = 0. \tag{9}$$

Here

$$\tilde{\rho}^{(2)} = [1 - \mathrm{i}b(y)]\rho, \quad \tilde{\rho}^{(3)} = [1 - \mathrm{i}b(z)]\rho\,,$$
$$\tilde{c}^{(2)}_{ijkl} = \begin{bmatrix} [1-\mathrm{i}b(y)]c_{1jk1} & c_{1jk2} & [1-\mathrm{i}b(y)]c_{1jk3} \\ c_{2jk1} & \dfrac{c_{2jk2}}{1-\mathrm{i}b(y)} & c_{2jk3} \\ [1-\mathrm{i}b(y)]c_{3jk1} & c_{3jk2} & [1-\mathrm{i}b(y)]c_{3jk3} \end{bmatrix},$$
$$\tilde{c}^{(3)}_{ijkl} = \begin{bmatrix} [1-\mathrm{i}b(z)]c_{1jk1} & [1-\mathrm{i}b(z)]c_{1jk2} & c_{1jk3} \\ [1-\mathrm{i}b(z)]c_{2jk1} & [1-\mathrm{i}b(z)]c_{2jk2} & c_{2jk3} \\ c_{3jk1} & c_{3jk2} & \dfrac{c_{3jk3}}{[1-\mathrm{i}b(z)]} \end{bmatrix}. \tag{10}$$

Note that the top of the model usually has a free-surface (zero stress) boundary condition. Therefore, the general form of the wave equation incorporating the PMLs may be rewritten as follows:

$$\frac{\partial}{\partial x_i}\left(\tilde{c}_{ijkl}\frac{\partial u_k}{\partial x_l}\right)+\tilde{\rho}\omega^2 u_j+f_j(\omega)\delta(\mathbf{r}-\mathbf{r}_s)=0,\qquad \mathbf{r},\mathbf{r}_s\in\Omega, \tag{11}$$

where the model parameters $\tilde{\mathbf{m}}=(\tilde{\rho},\tilde{c}_{ijkl})$ become

$$\begin{aligned}
\tilde{\rho}&=\rho[1-\mathrm{i}b(x)][1-\mathrm{i}b(y)][1-\mathrm{i}b(z)],\\
\tilde{c}_{1jk1}&=c_{1jk1}[1-\mathrm{i}b(y)][1-\mathrm{i}b(z)]/[1-\mathrm{i}b(x)],\\
\tilde{c}_{1jk2}&=c_{1jk2}[1-\mathrm{i}b(z)],\\
\tilde{c}_{1jk3}&=c_{1jk3}[1-\mathrm{i}b(y)],\\
\tilde{c}_{2jk1}&=c_{2jk1}[1-\mathrm{i}b(z)],\\
\tilde{c}_{2jk2}&=c_{2jk2}[1-\mathrm{i}b(x)][1-\mathrm{i}b(z)]/[1-\mathrm{i}b(y)],\\
\tilde{c}_{2jk3}&=c_{2jk3}[1-\mathrm{i}b(x)],\\
\tilde{c}_{3jk1}&=c_{3jk1}[1-\mathrm{i}b(y)],\\
\tilde{c}_{3jk2}&=c_{3jk2}[1-\mathrm{i}b(x)],\\
\tilde{c}_{3jk3}&=c_{3jk3}[1-\mathrm{i}b(x)][1-\mathrm{i}b(y)]/[1-\mathrm{i}b(z)].
\end{aligned} \tag{12}$$

These are obtained from a combination of eqs (8) and (10). Comparing eq. (12) with those given by Komatitsch & Tromp (2003) and Festa & Vilotte (2005), one can see the difference in that the density and the elastic moduli all become complex values and are not functions of the frequency. We call eq. (12) the 'PML-model parameters' that define the complex-valued density and elasticity modulus tensor, whose imaginary parts are specified by the functions $\{b(\xi),\ \xi=x,y,z\}$ in the PML and are valid for arbitrary anisotropic media. Comparing eq. (11) with eq. (1), one finds that the seismic wave equation incorporating the PMLs is the same as the original so that any numerical solver used for eq. (1) may be directly applied to eq. (11).

If the point-source spectrum is expressed by $f_j(\omega)=f(\omega)\hat{\mathbf{s}}$, where $\hat{\mathbf{s}}=(\hat{s}_1,\hat{s}_2,\hat{s}_3)$ is the unit vector, we may define the Green's function vector $\mathbf{G}^{(s)}=(G_1^{(s)},G_2^{(s)},G_3^{(3)})$ satisfying

$$\mathbf{D}(\tilde{\mathbf{m}})\mathbf{G}^{(s)}=-\hat{\mathbf{s}}\delta(\mathbf{r}-\mathbf{r}_s),\qquad \mathbf{r},\mathbf{r}_s\in\Omega. \tag{13}$$

Here $\mathbf{D}(\tilde{\mathbf{m}})$ is the differential operator given by

$$\mathbf{D}(\tilde{\mathbf{m}})\mathbf{G}^{(s)}=\left[\frac{\partial}{\partial x_i}\left(\tilde{c}_{ijkl}\frac{\partial G_k^{(s)}}{\partial x_l}\right)+\tilde{\rho}\omega^2 G_j^{(s)}\right]\mathbf{e}_j, \tag{14}$$

so that the displacement response $\mathbf{u}(\omega,\mathbf{r}_s,\mathbf{r})$ to any directed point-source may be obtained from

$$\mathbf{u}(\omega,\mathbf{r}_s,\mathbf{r})=f(\omega)\mathbf{G}^{(s)}(\omega,\mathbf{r}_s,\mathbf{r}). \tag{15}$$

Eq. (15) shows that the Green's function vector is the response of the displacement vector to a unit source vector. In a previous paper (Zhou & Greenhalgh 2009), we showed that such Green's function vectors $\mathbf{G}^{(s)}(\omega,\mathbf{r}_s,\mathbf{r})$ and $\mathbf{G}^{(g)}(\omega,\mathbf{r}_g,\mathbf{r})$ which correspond to unit source vectors at the source and geophone positions, are required for computing the sensitivity kernels and the Jacobian matrix in non-linear diffraction tomography and full-waveform inversion. Therefore, we prefer to use the Green's function vector $\mathbf{G}^{(s)}(\omega,\mathbf{r}_s,\mathbf{r})$ rather than the actual displacement vector $\mathbf{u}(\omega,\mathbf{r}_s,\mathbf{r})$ throughout the following text. Applying eq. (14), one can easily show that $\mathbf{D}(\tilde{\mathbf{m}})$ is a self-adjoint operator (Becker *et al*. 1983), which means that the following equation holds:

$$\langle\mathbf{G}^{(g)},\mathbf{D}(\tilde{\mathbf{m}})\mathbf{G}^{(s)}\rangle\ =\ \langle\mathbf{G}^{(s)},\mathbf{D}(\tilde{\mathbf{m}})\mathbf{G}^{(g)}\rangle \tag{16}$$

for any two Green's function vectors $\mathbf{G}^{(s)}$ and $\mathbf{G}^{(g)}\in C_0^2(\Omega)$. Here $\langle\ ,\ \rangle$ stands for the integral expression

$$\begin{aligned}
\langle\mathbf{G}^{(g)},\mathbf{D}(\tilde{\mathbf{m}})\mathbf{G}^{(s)}\rangle&=\int_\Omega G_j^{(g)}\left[\frac{\partial}{\partial x_i}\left(\tilde{c}_{ijkl}\frac{\partial G_k^{(s)}}{\partial x_l}\right)+\tilde{\rho}\omega^2 G_j^{(s)}\right]\mathrm{d}\Omega\\
&=\int_\Omega\left[\frac{\partial}{\partial x_i}\left(\tilde{c}_{ijkl}G_j^{(g)}\frac{\partial G_k^{(s)}}{\partial x_l}\right)-\tilde{c}_{ijkl}\frac{\partial G_j^{(g)}}{\partial x_i}\frac{\partial G_k^{(s)}}{\partial x_l}+\tilde{\rho}\omega^2 G_j^{(g)}G_j^{(s)}\right]\mathrm{d}\Omega\\
&=\int_{\partial\Omega}\mathbf{G}^{(g)}\cdot\boldsymbol{\sigma}^{(s)}(\mathbf{n})d\Gamma-\int_\Omega\left[\tilde{c}_{ijkl}\frac{\partial G_j^{(g)}}{\partial x_i}\frac{\partial G_k^{(s)}}{\partial x_l}-\tilde{\rho}\omega^2 G_j^{(g)}G_j^{(s)}\right]\mathrm{d}\Omega\\
&=-\int_\Omega\left[\tilde{c}_{ijkl}\frac{\partial G_j^{(g)}}{\partial x_i}\frac{\partial G_k^{(s)}}{\partial x_l}-\tilde{\rho}\omega^2 G_j^{(g)}G_j^{(s)}\right]\mathrm{d}\Omega.
\end{aligned} \tag{17}$$

In obtaining these results, we have used Gauss' theorem and the natural boundary conditions that $\mathbf{G}^{(g)}|_{\partial\Omega\to\infty} = 0$ and $\boldsymbol{\sigma}^{(s)}(\mathbf{n}) = \tilde{c}_{ijkl}\partial G_k^{(s)}/\partial x_l = \mathbf{0}$ on the free-surface boundary $\partial\Omega$. Substituting eq. (13) into (16), one has the Reciprocity Principle

$$\hat{\mathbf{s}} \cdot \mathbf{G}^{(g)}(\mathbf{r}_g, \mathbf{r}_s) = \hat{\mathbf{g}} \cdot \mathbf{G}^{(s)}(\mathbf{r}_s, \mathbf{r}_g). \tag{18}$$

To solve eq. (13), we may apply the Variational Principle to convert it into minimization of the functional integration (weak form of solution of the PDE, see Becker *et al*. 1983).

$$\min_{\mathbf{G}^{(s)}\in\mathbf{C}_0^1(\Omega)}\{\ \Psi(\mathbf{G}^{(s)})\} = \min_{\mathbf{G}^{(s)}\in\mathbf{C}_0^1(\Omega)} \left\{ \frac{1}{2}\left\langle \mathbf{G}^{(s)}, \mathbf{D}(\tilde{\mathbf{m}})\mathbf{G}^{(s)}\right\rangle - \left\langle \mathbf{G}^{(s)}, -\hat{\mathbf{s}}\delta(\mathbf{r}-\mathbf{r}_s)\right\rangle \right\} \tag{19}$$

because of the perturbation formula and the self-adjoint property of $\mathbf{D}(\tilde{\mathbf{m}})$

$$\begin{aligned}
\delta\Psi &= \frac{1}{2}\left[\left\langle \delta\mathbf{G}^{(s)}, \mathbf{D}(\tilde{\mathbf{m}})\mathbf{G}^{(s)}\right\rangle + \left\langle \mathbf{G}^{(s)}, \mathbf{D}(\tilde{\mathbf{m}})\delta\mathbf{G}^{(s)}\right\rangle\right] - \left\langle \delta\mathbf{G}^{(s)}, -\hat{\mathbf{s}}\delta(\mathbf{r}-\mathbf{r}_s)\right\rangle \\
&= \frac{1}{2}\left[\left\langle \delta\mathbf{G}^{(s)}, \mathbf{D}(\tilde{\mathbf{m}})\mathbf{G}^{(s)}\right\rangle + \left\langle \delta\mathbf{G}^{(s)}, \mathbf{D}(\tilde{\mathbf{m}})\mathbf{G}^{(s)}\right\rangle\right] - \left\langle \delta\mathbf{G}^{(s)}, -\hat{\mathbf{s}}\delta(\mathbf{r}-\mathbf{r}_s)\right\rangle \\
&= \left\langle \delta\mathbf{G}^{(s)}, \mathbf{D}(\tilde{\mathbf{m}})\mathbf{G}^{(s)}\right\rangle - \left\langle \delta\mathbf{G}^{(s)}, -\hat{\mathbf{s}}\delta(\mathbf{r}-\mathbf{r}_s)\right\rangle \\
&= \left\langle \delta\mathbf{G}^{(s)}, \mathbf{D}(\tilde{\mathbf{m}})\mathbf{G}^{(s)} + \hat{\mathbf{s}}\delta(\mathbf{r}-\mathbf{r}_s)\right\rangle = 0,
\end{aligned} \tag{20}$$

which shows $\delta\Psi$ vanishes if only if eq. (13) is satisfied for any perturbation $\delta\mathbf{G}^{(s)}$.

NUMERICAL IMPLEMENTATION

Consider a 3-D computational domain Ω given by $[x_{\min}, x_{\max}]\times\ [y_{\min}, y_{\max}]\ [0,\ z_0(x, y)]$ (similarly for a spherical domain $[\varphi_{\min}, \varphi_{\max}] \times [\theta_{\min}, \theta_{\max}]\times\ [r_{\min}, r_0(\varphi, \theta)]$), where $z_0(x, y)$ or $r_0(\theta, \varphi)$ is the free-surface topography of the Earth (see Fig. 1). We discretize the domain with the points: $x_{\min} = x_1 < x_2 < \ldots < x_{N_x} = x_{\max}$, $y_{\min} = y_1 < y_2 < \ldots < y_{N_y} = y_{\max}$ in the xy-plane and the interfaces of the layers, if the model includes them or as pure mathematical boundaries if the model does not: $0 \le z_k(x, y) \le z_0(x, y)$, $(k = 1, 2, \ldots, N_z)$ in the vertical direction. There exists a set of sub-domains $\{\Omega_p, p = 1, 2, \ldots, (N_x - 1)(N_y - 1)(N_z - 1)$ defined by $[x_{i-1}, x_i] \times [y_{j-1}, y_j] \times [z_{k-1}(x, y), z_k(x, y)]$, to which the following coordinate transformation may be applied:

$$\begin{cases}
x = \dfrac{(x_i - x_{i-1})}{2}\xi + \dfrac{(x_{i-1} + x_i)}{2}, & \xi \in [-1, 1], \\
y = \dfrac{(y_j - y_{j-1})}{2}\eta + \dfrac{(y_{j-1} + y_j)}{2}, & \eta \in [-1, 1], \\
z = \dfrac{[z_k(x, y) - z_{k-1}(x, y)]}{2}\varsigma + \dfrac{[z_{k-1}(x, y) + z_k(x, y)]}{2}, & \varsigma \in [-1, 1].
\end{cases} \tag{21}$$

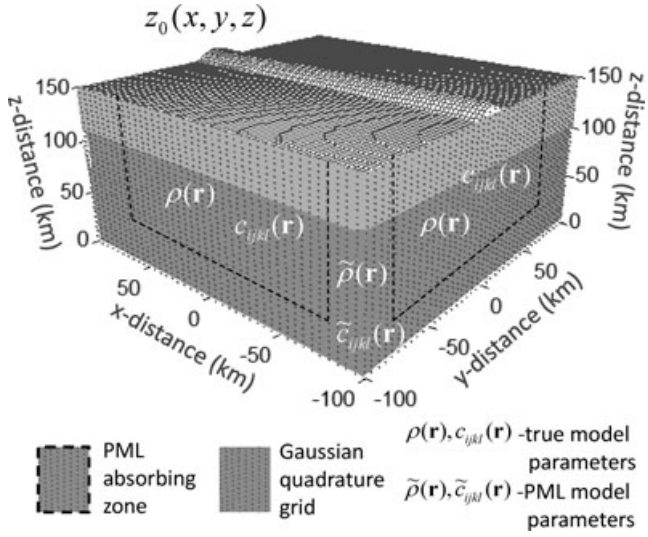

Figure 1. Sketch of a 3-D Gaussian quadrature grid that samples the model parameters $\mathbf{m} = (\rho, c_{ijkl})$, matches the free-surface $z_0(x, y)$ and incorporates the perfectly matched layers (PML) in 3-D seismic wave modelling.

Taking derivatives, we obtain

$$\begin{cases} \dfrac{\partial x}{\partial \xi} = \dfrac{1}{2}(x_i - x_{i-1}) = \dfrac{\Delta x_i}{2}, \qquad \dfrac{\partial y}{\partial \eta} = \dfrac{1}{2}(y_j - y_{j-1}) = \dfrac{\Delta y_j}{2}, \\ \dfrac{\partial z}{\partial x} = \dfrac{1}{2}\left[\dfrac{\partial z_k(x,y)}{\partial x} - \dfrac{\partial z_{k-1}(x,y)}{\partial x}\right]\varsigma + \dfrac{1}{2}\left[\dfrac{\partial z_{k-1}(x,y)}{\partial x} + \dfrac{\partial z_k(x,y)}{\partial x}\right], \\ \dfrac{\partial z}{\partial y} = \dfrac{1}{2}\left[\dfrac{\partial z_k(x,y)}{\partial y} - \dfrac{\partial z_{k-1}(x,y)}{\partial x}\right]\varsigma + \dfrac{1}{2}\left[\dfrac{\partial z_{k-1}(x,y)}{\partial x} + \dfrac{\partial z_k(x,y)}{\partial x}\right], \\ \dfrac{\partial z}{\partial \varsigma} = \dfrac{1}{2}[z_k(x,y) - z_{k-1}(x,y)] = \dfrac{\Delta z_k(x,y)}{2}. \end{cases} \tag{22}$$

The Jacobian determinant is given by

$$J^p = \frac{\partial(x,y,z)}{\partial(\xi,\eta,\varsigma)} = \frac{1}{8}\Delta x_i \Delta y_j \Delta z_k(x,y). \tag{23}$$

The sub-domain integration may be easily calculated by applying the Gaussian quadrature formula, that is

$$\frac{1}{2}\int_{\Omega_p}\left(\tilde{c}_{ijkl}\frac{\partial G_k^{(s)}}{\partial x_l}\frac{\partial G_j^{(s)}}{\partial x_i} - \tilde{\rho}\omega^2 G_j^{(s)} G_j^{(s)}\right)\mathrm{d}\Omega = \frac{1}{2}w_\nu^p\left[\left(\tilde{c}_{ijkl}\frac{\partial G_k^{(s)}}{\partial x_l}\frac{\partial G_j^{(s)}}{\partial x_i} - \tilde{\rho}\omega^2 G_j^{(s)} G_j^{(s)}\right)|J^p|\right]_\nu . \tag{24}$$

Here, the subscript $\nu = (\gamma-1)n_\xi n_\eta + (\beta-1)n_\xi + \alpha$ stands for the Gaussian quadrature abscissae $\{(\xi_\alpha, \eta_\beta, \varsigma_\gamma), 1 \le \alpha \le n_\xi, 1 \le \beta \le n_\eta, 1 \le \gamma \le n_\varsigma\}$ at which the Gaussian weights w_ν^p are applied. The abscissa and weights depend on different Gaussian quadrature schemes, such as the Gauss-Lobbatto scheme (Phillip & Rabinowitz 1984), or an error function-based quadrature scheme (Crandall 1996), or a tanh-sinh quadrature scheme (Takahasi & Mori 1974). The three integers n_ξ, n_η and n_ς are the local numbers of the Gaussian quadrature abscissae in the three directions, and the global numbers in each direction can been found from the expressions $N_\xi = (N_x - 1)n_\xi + 1$, $N_\eta = (N_y - 1)n_\eta + 1$ and $N_\varsigma = (N_z - 1)n_\varsigma + 1$. Once n_ξ, n_η and n_ς are given, one can calculate the abscissae $(\xi_\alpha, \eta_\beta, \varsigma_\gamma)$ and weights w_ν^n in terms of the Gaussian quadrature schemes so that the positions of the quadrature points in Ω_p can be found by eq. (21). All the Gaussian abscissae form a point-by-point grid spanning the global domain for description of the model geology and computation of the integrals, so we call the method the GQG approach. We prefer to name Ω_p the 'sub-domains' rather than the 'elements' because there are several important differences. The sub-domains Ω_p are treated purely as integral sub-volumes and are not related to the specific physical properties of the model, or the model parametrization. Eq. (24) shows that sampling the model parameter is fulfilled by means of the Gaussian quadrature points ν (point-gridded model) rather than employing hexahedral elements (hexahedral meshed model) which is common in the SEM. Therefore, we actually replace the hexahedral element mesh with the point-gridded mesh so that parametrizing the model and matching complex topography of the free-surface and sub-surface interfaces become simpler and more refined (see Fig. 1). From Gaussian quadrature theory, the abscissae $(\xi_\alpha, \eta_\beta, \varsigma_\gamma)$ and the weights w_ν^n may be determined from the known topography $z_0(x, y)$, the interfaces or mathematical boundaries $z_k(x, y)$ of the earth model, and the number of abscissae values $\{n_\xi, n_\eta, n_\varsigma\}$. The latter dominates the accuracy of the integration and may be determined from the number of points per minimum wavelength of the waves being simulated. Bailey *et al*. (2005) have demonstrated the high precision of applying three Gaussian quadrature schemes (Gauss-Lobbatto, an error function-based scheme, and a tanh-sinh quadrature scheme) to a large class of integrals, which involve continuous and well-behaved functions, continuous functions on finite intervals but with infinite derivatives at an endpoint, functions having an integrable singularity at the endpoint and oscillatory functions on an infinite interval. They showed that an appropriate number of Gaussian quadrature points may yield satisfactory precision of the integrals ($10^{-5} \sim 10^{-405}$). This means that the accuracy of the integration can be guaranteed with the Gaussian quadrature schemes.

Eq. (24) also shows that it is crucial to evaluate the tensor products $\tilde{c}_{ijkl}\partial G_k^{(s)}/\partial x_l \partial G_j^{(s)}/\partial x_i$ at the Gaussian quadrature abscissa. Due to the symmetric property of the elastic moduli tensor $\tilde{c}_{ijkl}$, there are (at most) 21 terms for the tensor products, which involve the gradient of the Green's function vector $\nabla \mathbf{G}^{(s)} = (\partial \mathbf{G}^{(s)}/\partial x, \partial \mathbf{G}^{(s)}/\partial y, \partial \mathbf{G}^{(s)}/\partial z)$. To calculate the gradients, we apply the differential chain rule

$$\begin{cases} \dfrac{\partial \mathbf{G}^{(s)}}{\partial x} = \left(\dfrac{2}{\Delta x_i}\right)\left(\dfrac{\partial \mathbf{G}^{(s)}}{\partial \xi}\right) - \left(\dfrac{\partial z}{\partial x}\right)\left(\dfrac{2}{\Delta z_k(x,y)}\right)\dfrac{\partial \mathbf{G}^{(s)}}{\partial \varsigma}, \\ \dfrac{\partial \mathbf{G}^{(s)}}{\partial y} = \left(\dfrac{2}{\Delta y_j}\right)\left(\dfrac{\partial \mathbf{G}^{(s)}}{\partial \eta}\right) - \left(\dfrac{\partial z}{\partial y}\right)\left(\dfrac{2}{\Delta z_k(x,y)}\right)\dfrac{\partial \mathbf{G}^{(s)}}{\partial \varsigma}, \\ \dfrac{\partial \mathbf{G}^{(s)}}{\partial z} = \left(\dfrac{2}{\Delta z_k(x,y)}\right)\left(\dfrac{\partial \mathbf{G}^{(s)}}{\partial \varsigma}\right), \end{cases} \tag{25}$$

where $\partial z/\partial x$ and $\partial z/\partial y$ are given by eq. (22).

In a sub-domain Ω_p, the Green's function vector $\mathbf{G}_\nu^{(s,p)} = (G_{x\nu}^{(s,p)}, G_{y\nu}^{(s,p)}, G_{z\nu}^{(s,p)})$ at the Gaussian quadrature abscissae ν may be expressed by the Lagrange interpolation formula

$$\mathbf{G}_\nu^{(s,p)} = l_\alpha(\xi) l_\beta(\eta) l_\gamma(\varsigma) \mathbf{G}_{\alpha\beta\gamma}^{(s,p)}, \ \ \nu = (\alpha-1)n_\varsigma n_\eta + (\beta-1)n_\varsigma + \gamma, \tag{26}$$

which gives the derivatives

$$\frac{\partial \mathbf{G}_{\nu}^{(s,p)}}{\partial \xi} = l'_{\alpha}(\xi) l_{\beta}(\eta) l_{\gamma}(\varsigma) \mathbf{G}_{\alpha\beta\gamma}^{(s,p)},$$
$$\frac{\partial \mathbf{G}_{\nu}^{(s,p)}}{\partial \eta} = l_{\alpha}(\xi) l'_{\beta}(\eta) l_{\gamma}(\varsigma) \mathbf{G}_{\alpha\beta\gamma}^{(s,p)},$$
$$\frac{\partial \mathbf{G}_{\nu}^{(s,p)}}{\partial \varsigma} = l_{\alpha}(\xi) l_{\beta}(\eta) l'_{\gamma}(\varsigma) G_{\alpha\beta\gamma}^{(s,p)}, \quad \nu = (\alpha - 1) n_{\varsigma} n_{\eta} + (\beta - 1) n_{\varsigma} + \gamma. \tag{27}$$

Substituting eq. (26) for the second term in the RHS of eq. (24), we get

$$\omega^2 w_{\nu}^{p} (\tilde{\rho} G_{j}^{(s,p)} G_{j}^{(s,p)})_{\mathbf{r}_{\nu}}$$
$$= (G_{x\nu}^{(s,p)}, G_{y\nu}^{(s,p)}, G_{y\nu}^{(s,p)}) \begin{pmatrix} \omega^2 \tilde{\rho}_{\nu} w_{\nu}^{p} & 0 & 0 \\ 0 & \omega^2 \tilde{\rho}_{\nu} w_{\nu}^{p} & 0 \\ 0 & 0 & \omega^2 \tilde{\rho}_{\nu} w_{\nu}^{p} \end{pmatrix} \begin{pmatrix} G_{x\nu}^{(s,p)} \\ G_{y\nu}^{(s,p)} \\ G_{z\nu}^{(s,p)} \end{pmatrix} \tag{28}$$
$$= [\mathbf{G}_{\nu}^{(s,p)}]^T \mathbf{D}_0^e \mathbf{G}_{\nu}^{(s,p)},$$

where

$$\mathbf{D}_0^p = \mathrm{diag}\{(\omega^2 \rho_{\nu} w_{\nu}^{p}, \omega^2 \rho_{\nu} w_{\nu}^{p}, \omega^2 \rho_{\nu} w_{\nu}^{p})\}. \tag{29}$$

Substitution of eq. (27) into (25), gives the matrix form of the derivatives

$$\frac{\partial \mathbf{G}^{(s,p)}}{\partial x} = \left(\frac{\partial G_x^{(s,p)}}{\partial x}, \frac{\partial G_y^{(s,p)}}{\partial x}, \frac{\partial G_z^{(s,p)}}{\partial x} \right) = \mathbf{D}_x [\mathbf{G}_x^{(s,p)}, \mathbf{G}_y^{(s,p)}, \mathbf{G}_z^{(s,p)}],$$
$$\frac{\partial \mathbf{G}^{(s,p)}}{\partial y} = \left(\frac{\partial G_x^{(s,p)}}{\partial y}, \frac{\partial G_y^{(s,p)}}{\partial y}, \frac{\partial G_z^{(s,p)}}{\partial y} \right) = \mathbf{D}_y [\mathbf{G}_x^{(s,p)}, \mathbf{G}_y^{(s,p)}, \mathbf{G}_z^{(s,p)}],$$
$$\frac{\partial \mathbf{G}^{(s,p)}}{\partial z} = \left(\frac{\partial G_x^{(s,p)}}{\partial y}, \frac{\partial G_y^{(s,p)}}{\partial y}, \frac{\partial G_z^{(s,p)}}{\partial y} \right) = \mathbf{D}_z [\mathbf{G}_x^{(s,p)}, \mathbf{G}_y^{(s,e)}, \mathbf{G}_z^{(s,p)}], \tag{30}$$

where

$$\mathbf{G}_{\chi}^{(s,p)} = (G_{\chi 1}^{(s,p)}, G_{\chi 2}^{(s,p)}, G_{\chi 3}^{(s,p)}, \ldots, G_{\chi \nu}^{(s,p)}, \ldots, G_{\chi N}^{(s,p)}), \ (\chi = x, y, z),$$

$$\mathbf{D}_x = \left[\frac{2}{\Delta x_i} l'_1(\xi), \frac{2}{\Delta x_i} l'_2(\xi), \ldots, \frac{2}{\Delta x_i} l'_{N_{\xi}}(\xi), \frac{2}{\Delta z_k(x,y)} \frac{\partial z}{\partial x} l'_1(\varsigma), \right.$$
$$\left. \frac{2}{\Delta z_k(x,y)} \frac{\partial z}{\partial x} l'_2(\varsigma), \ldots, \frac{2}{\Delta z_k(x,y)} \frac{\partial z}{\partial x} l'_{N_{\varsigma}}(\varsigma) \right],$$

$$\mathbf{D}_y = \left[\frac{2}{\Delta y_j} l'_1(\eta), \frac{2}{\Delta y_j} l'_2(\eta), \ldots, \frac{2}{\Delta y_j} l'_{N_{\eta}}(\eta), \frac{2}{\Delta z_k(x,y)} \frac{\partial z}{\partial y} l'_1(\varsigma), \right.$$
$$\left. \frac{2}{\Delta z_k(x,y)} \frac{\partial z}{\partial y} l'_2(\varsigma), \ldots, \frac{2}{\Delta z_k(x,y)} \frac{\partial z}{\partial y} l'_{N_{\varsigma}}(\varsigma) \right], \tag{31}$$

$$\mathbf{D}_z = \left[\frac{2}{\Delta z_k(x,y)} l'_1(\varsigma), \frac{2}{\Delta z_k(x,y)} l'_2(\varsigma), \ldots, \frac{2}{\Delta z_k(x,y)} \frac{\partial z}{\partial x} l'_{N_{\varsigma}}(\varsigma) \right].$$

Due to application of the Gaussian quadrature abscissae for the differential operators $\mathbf{D}_x$, $\mathbf{D}_y$ and $\mathbf{D}_z$, the differentiations given by eqs (30) and (31) have exponential convergence in terms of the spectral method theory. Trefethen (2000) has shown such exponential convergence for spatial differentiation on smooth functions when using the 'Chebyshev points'. This includes the Gaussian quadrature abscissa, so that such an approach is superior to the traditional finite difference and finite-element methods. In a general anisotropic solid there are 21 independent elastic moduli, so the first term (tensor product) in eq. (24) has the following expansion:

$$\tilde{c}_{ijkl} \frac{\partial G_k^{(s,p)}}{\partial x_l} \frac{\partial G_j^{(s,p)}}{\partial x_i} = (\mathbf{G}_x^{(s,p)})^T \mathbf{A}_1^p \mathbf{G}_x^{(s,p)} + (\mathbf{G}_y^{(s,p)})^T \mathbf{A}_2^p \mathbf{G}_y^{(s,p)} + (\mathbf{G}_z^{(s,p)})^T \mathbf{A}_3^p \mathbf{G}_z^{(s,p)}$$
$$+ (\mathbf{G}_x^{(s,p)})^T \mathbf{A}_4^p \mathbf{G}_y^{(s,p)} + (\mathbf{G}_x^{(s,p)})^T \mathbf{A}_5^p \mathbf{G}_z^{(s,p)} + (\mathbf{G}_y^{(s,p)})^T \mathbf{A}_6^p \mathbf{G}_z^{(s,p)}. \tag{32}$$

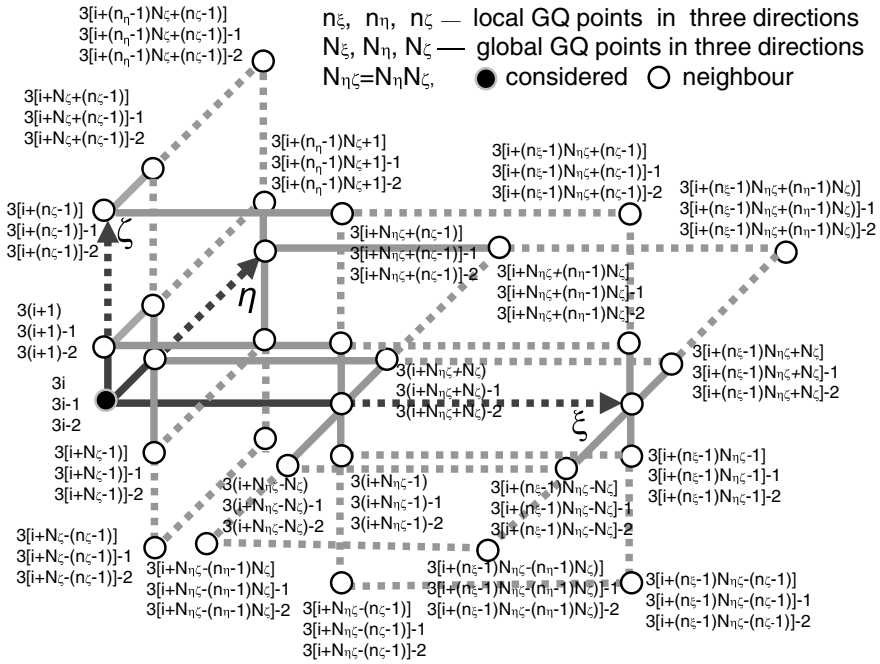

Figure 2. The neighbouring points of the *i*th Gaussian quadrature abscissa that contribute to the non-zero elements of each row in the resulting linear-system matrix.

The matrices $\{\mathbf{A}_1^p, \mathbf{A}_2^p, \mathbf{A}_3^p, \mathbf{A}_4^p, \mathbf{A}_5^p, \mathbf{A}_6^p\}$ are given in the Appendix; they are symmetric differential matrices at the Gaussian quadrature abscissae.

Substituting eqs (28) and (32) into (24), we obtain the quadratic version of the functional integral

$$\Psi(\mathbf{G}^{(s)}) = \frac{1}{2}\mathbf{G}^{(s)^T}\mathbf{A}\mathbf{G}^{(s)} - \mathbf{b}_s\mathbf{G}^{(s)}, \tag{33}$$

where $\mathbf{G}^{(s)^T} = (G_{x1}^{(s)}, G_{y1}^{(s)}, G_{z1}^{(s)}, \ldots, G_{xN}^{(s)}, G_{yN}^{(s)}, G_{zN}^{(s)})$ is the global Green's function vector whose components are the vector values at the Gaussian quadrature abscissa $\nu = 1,2,\ldots N$; $\mathbf{b}_s = (\mathbf{0},\mathbf{0},\ldots,\hat{\mathbf{s}},\mathbf{0},\ldots\mathbf{0})$ is the source vector whose components are zero except at the source location, and $\mathbf{A} = \sum_{p,k,\nu}[\mathbf{D}_0^p + w_\nu^p(|J^p|\mathbf{A}_k^p)_\nu]$ is the global system matrix assembled with the sub-domain matrices given by eq. (31) and elaborated in the Appendix. Therefore, the Green's function vector $\mathbf{G}^{(s)}$ may be obtained by solving the linear equation system for every separate frequency.

$$\mathbf{A}\mathbf{G}^{(s)} = \mathbf{b}_s. \tag{34}$$

From the differential matrices given in the Appendix, one can see that the global matrix $\mathbf{A}$ in eq. (34) is symmetric, sparse and banded, so it is necessary to only calculate the upper part or the lower part and store the non-zero elements in compressed half-row storage; this reduces the computer memory requirement for a 3-D model. According to eq. (31), we can draw Fig. 2 which shows the neighbouring points corresponding to the upper part $\{A_{ij}, j \geq i\}$ of the matrix $\mathbf{A}$ at the *i*th Gaussian quadrature abscissa. It gives the maximum number (width of the band) of the non-zero elements in each row of the upper part of $\mathbf{A}$.

$$\begin{aligned} N_{\text{row}} = {} & 3\{n_\varsigma + (n_\eta - 1)[2(n_\varsigma - 1) + 1] + (n_\xi - 1)[2(n_\eta - 1) + 2(n_\varsigma - 1) + 1]\} + \\ & 2\{(n_\eta - 1) + (n_\xi - 1)[2(n_\eta - 1) + 1]\}. \end{aligned} \tag{35}$$

Here the first bracket $\{\}$ on the RHS of eq. (35) gives the total number of related points to the *i*th Gaussian quadrature abscissa and the factor of 3 signifies all three components of the displacement vector at each point; the second bracket $\{\}$ gives the number of starting points in the ς-direction, except for the considered point (see Fig. 2) at which two extra column-indices must be defined due to there being three components at the *i*th Gaussian quadrature abscissa.

Applying a linear-system solver (Henk 2003), one may obtain the Green's function vector $\mathbf{G}^{(s)}$ throughout the 3-D anisotropic model, which is defined by $\mathbf{m} = \{\rho, c_{ijkl}\}$. Note that the matrix $\mathbf{A}$ given in eq. (34) differs from the one which arises in time-domain modelling. The latter is diagonal or tri-diagonal due to the second-order time marching scheme that is usually applied (i.e. see Komatitsch & Vilotte 1998). Solving a diagonal or tri-diagonal matrix is in general much more efficient than solving a banded matrix such as that given by eq. (34). This implies that to compute the seismograms, which involves successive wavefields over the entire time sequence (or the wavefields over the whole frequency range), the time-domain modelling method is more suitable than the frequency-domain modelling method, unless solving eq. (34) becomes competitive to the time-domain method, that is, applying an advanced parallelized solver to eq. (34) (Henk 2003). With a

direct matrix solver, the multiple source problem (different right-hand sides of eq. 34) is efficient because it involves simple vector-matrix multiplication once the inverse is found. However, memory requirements are considerable compared to the time-domain explicit approach. Therefore, the presented method is currently not intended for computing the time-domain seismograms. Rather, it is aimed at calculating the seismic wavefields for a few (dominant or well chosen) frequencies required in non-linear diffraction tomography (Gelius 1995) or frequency-domain full-waveform inversion (Pratt 1999), or in examining the sensitivity of the spectral data to each of the model parameters (Zhou & Greenhalgh 2009). Therefore, in the following section, we just give some illustrative computed wavefields at a specified single frequency. The method is nevertheless valid for any other frequencies and could be extended to a wide band of frequencies.

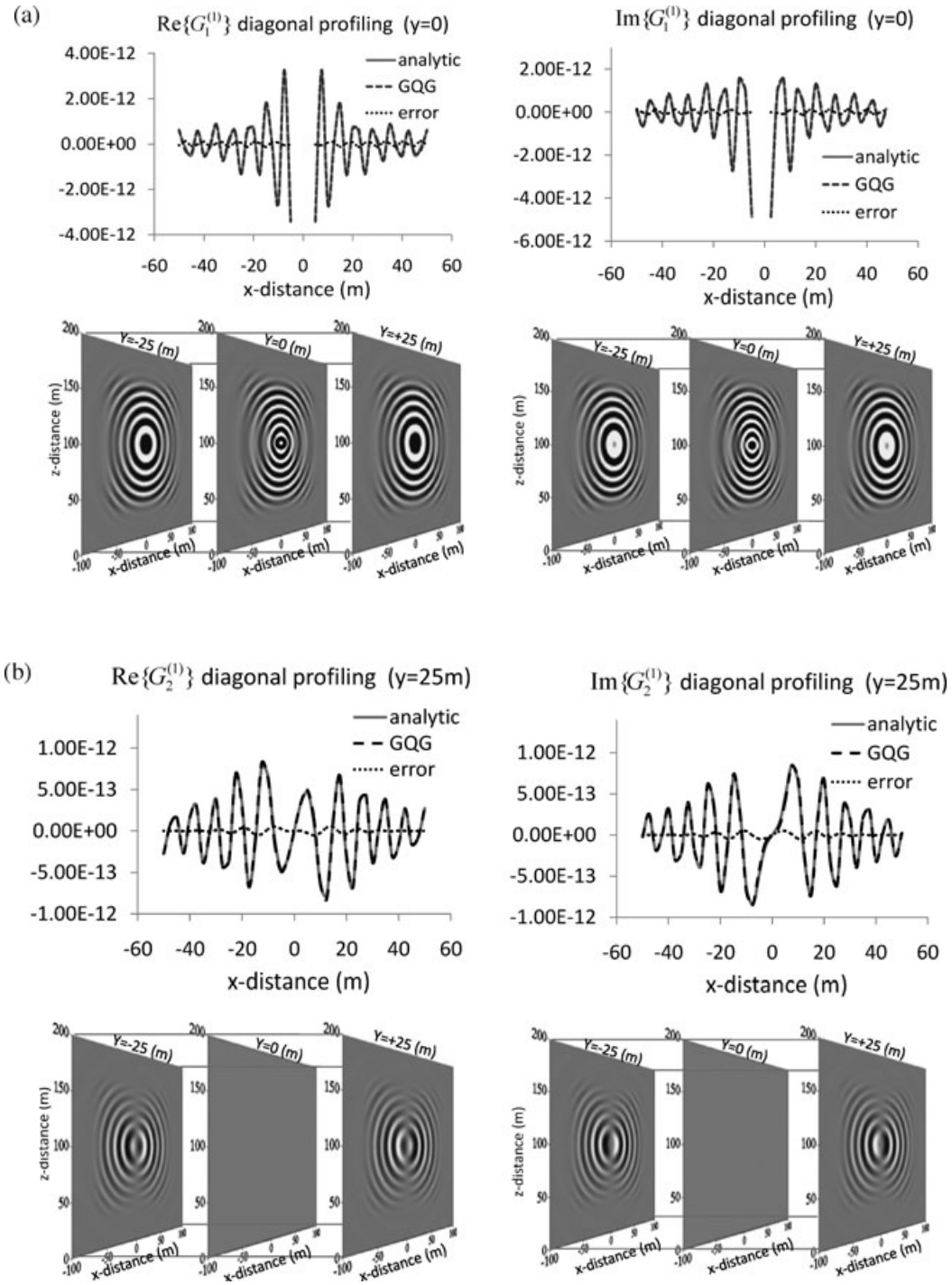

Figure 3. Six independent components of the GQG solutions for a 3-D full-space homogeneous isotropic medium ($\rho = 1000\ \mathrm{kg\,m^{-3}}$, $V_p = 2500\ \mathrm{m\,s^{-1}}$, $V_s = 1000\ \mathrm{m\,s^{-1}}$). (a) $G_1^{(1)}$-component, (b) $G_2^{(1)}$-component, (c) $G_3^{(1)}$-component, (d) $G_2^{(2)}$-component, (e) $G_3^{(2)}$-component and (f) $G_3^{(3)}$-component.

NUMERICAL EXAMPLES

To validate and test the accuracy of the GQG approach, we have carried out numerical simulations in two full-space homogenous, isotropic ($\rho = 1000\,\mathrm{kg\,m^{-3}}$, $V_p = 2500\,\mathrm{ms^{-1}}$, $V_p = 1000\,\mathrm{m\,s^{-1}}$) and anisotropic models ($\rho = 1000\,\mathrm{kg\,m^{-3}}$, $c_{11} = c_{33} = 6.25 \times 10^9$, $c_{13} = 4.25 \times 10^9$, $c_{44} = 1.0 \times 10^9$, $c_{66} = 1.0 \times 10^9\ \mathrm{kg\,m^{-1}\,s^{-2}}$), whose analytic solutions are given by Aki & Richards (1980) and Vavrycuk (2007), respectively. In the computations, we set up the 3-D domain of dimensions 200 m × 200 m × 200 m and employ three unit point-source vectors $\hat{\mathbf{s}}^{(1)} = (1, 0, 0)$, $\hat{\mathbf{s}}^{(2)} = (0,1,0)$ and $\hat{\mathbf{s}}^{(3)} = (0,0,1)$ located at the centre of the domain, and having a frequency of 100 Hz. From the model parameters and the given frequency, one finds that the minimum and maximum wavelengths of the simulated waves are 10 m and 25 m, respectively. The minimum wavelength is helpful to choose an appropriate number of Gaussian quadrature sampling points in the spatial domain. The maximum wavelength is used to determine the width of the PMLs. According to our previous 2.5-D wave modelling with the GQG approach, the required sampling density (N_G = number of points over the minimum wavelength) of the Gaussian quadrature abscissae should be more than five points per minimum wavelength. Therefore, any sampling density $N_G > 5$ per 10 m guaranties the modelling

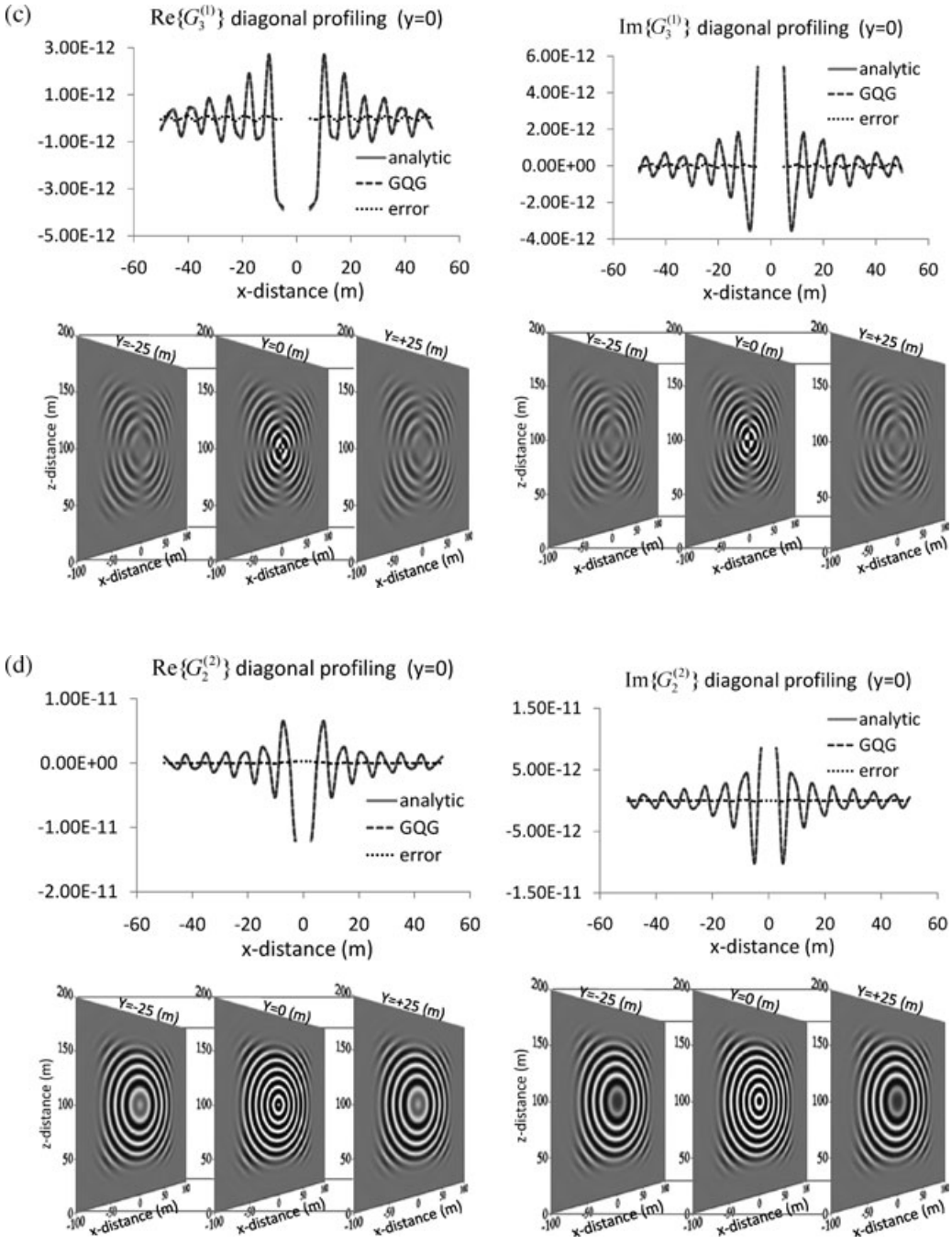

Figure 3. (*Continued.*)

accuracy. After choosing the sampling density, we conducted numerical experiments and found that the width of the PML should be larger than the maximum wavelength, that is, from one to two times the maximum wavelength, and incorporating the simple linear absorbing function $b(\xi) = |\xi - \xi_a|/|\xi_b - \xi_a|$, where ξ_a and ξ_b are the two end boundary points of the PML. This yields satisfactory results.

Note that for the same sampling density N_G, one may have options to choose the points $\{n_\xi, n_\eta, n_\varsigma\}$ in terms of the sub-domain dimensions $\{\Delta x_i, \Delta y_j, \Delta z_k(x, y)\}$, because of the relationship $N_G = \min\{n_\xi, n_\eta, n_\varsigma\}/\max\{\Delta x_i, \Delta y_j, \Delta z_k(x, y)\}$, that is, for $N_G = 5$ per 10 m, one has $\min\{n_\xi, n_\eta, n_\varsigma\} = 5$ and $\max\{\Delta x_i, \Delta y_j, \Delta z_k(x, y)\} = 10$, or $\min\{N^e_\xi, N^e_\eta, N^e_\varsigma\} = 10$ and $\max\{\Delta x_i, \Delta y_j, \Delta z_k(x, y)\} = 20$, both may be applied to discretize the model domain in terms of the model geometry and yield similar results. However, it should be mentioned that employing a large number of Gaussian quadrature abscissae $\{n_\xi, n_\eta, n_\varsigma\}$ will increase the non-zero elements in each row of the system matrix A (see eq. 35) and therefore costs more computer time and memory. It is very similar to the situation of the spectral method in which the number of collocation points is increased (Trefethen 2000). Accordingly, to guarantee the accuracy we choose $N_G = 3$ per 2.5 m (or 9 points per 10 m) and create a GQG of $161 \times 161 \times 161$ nodes sampling the model parameters and obtain a sparse, symmetric complex matrix

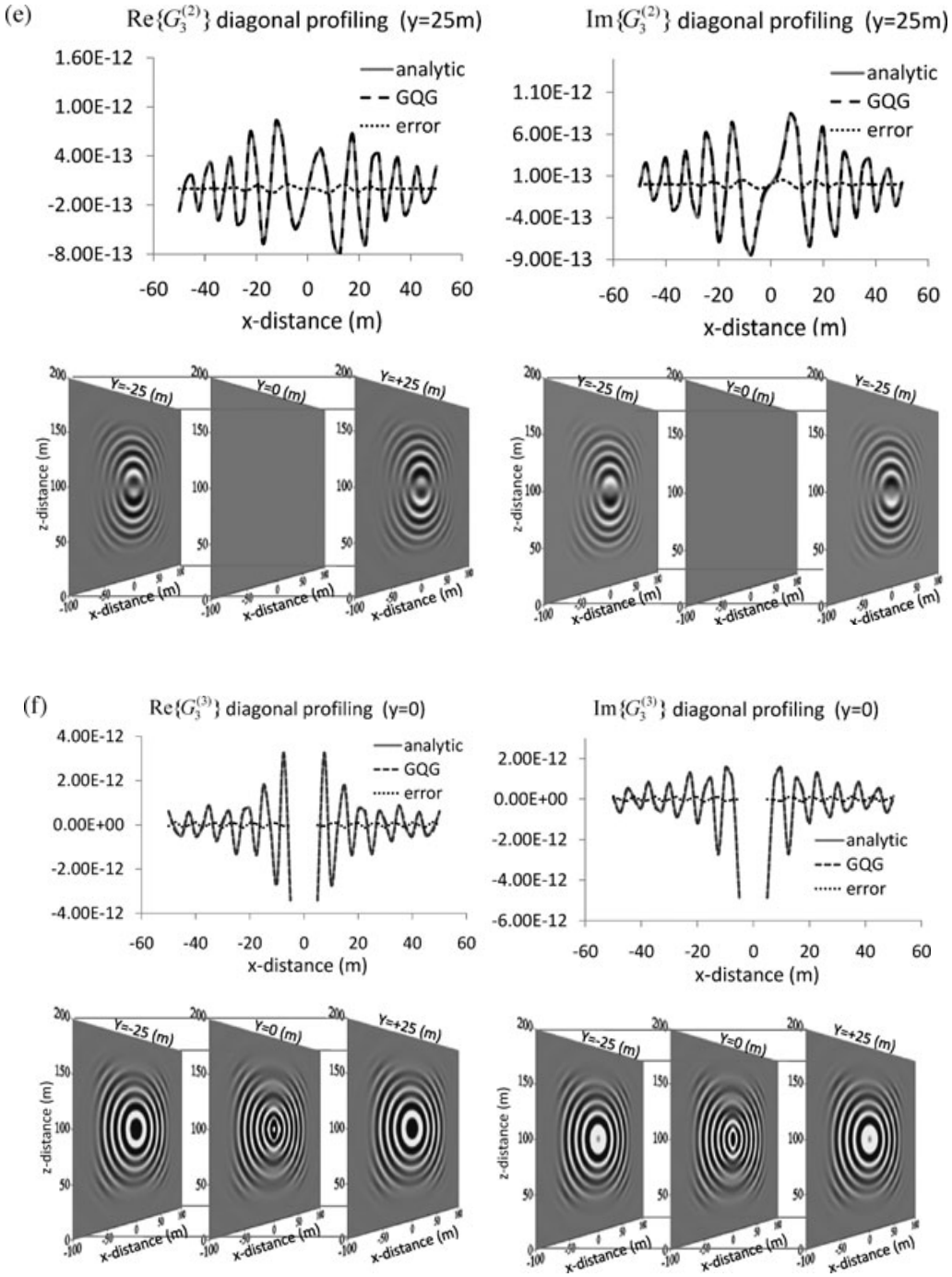

Figure 3. (*Continued.*)

A of 12 519 843 × 12 519 843 (see eq. 34), which is stored in the manner of 'compressed half-row storage'—three arrays A(∗), IA(∗) and JA(∗) hold all the non-zero elements of the upper part $\{A_{ij}, j \geq i\}$ and their row- and column-index. Here, IA(∗) gives the number of non-zero elements of each half row ($j \geq i$) and JA(∗) holds the column index of the non-zero elements stored in A(∗). Obviously, it requires the least computer memory (about 31 GB for the two 3-D cases). It is desirable that eq. (34) should be solved by a parallelized solver with such a least-memory storage scheme (Henk 2003). Unfortunately, to date we have not found any available version of the parallelized solver using the compressed half-row storage scheme. The parallelized direct solvers, such as SuperLU (Li & Demmel 2003) and PARDISO (Schenk & Gärtner 2004), require huge memory for such 3-D modelling due to the LU factorization (lower and upper triangular decomposition). Sinclair (2009) has shown that the memory requirements of SuperLU and PARDISO rapidly increase with the number of non-zero elements entries in the matrix A. Such ravenous appetites of the direct solvers make them unsuitable for the 3-D frequency-domain modelling. Some other parallelized iterative solver packages, for example, PSBLAS (Filippone & Colajanni 2000) and LIS (Fujii *et al*. 2007) have been developed

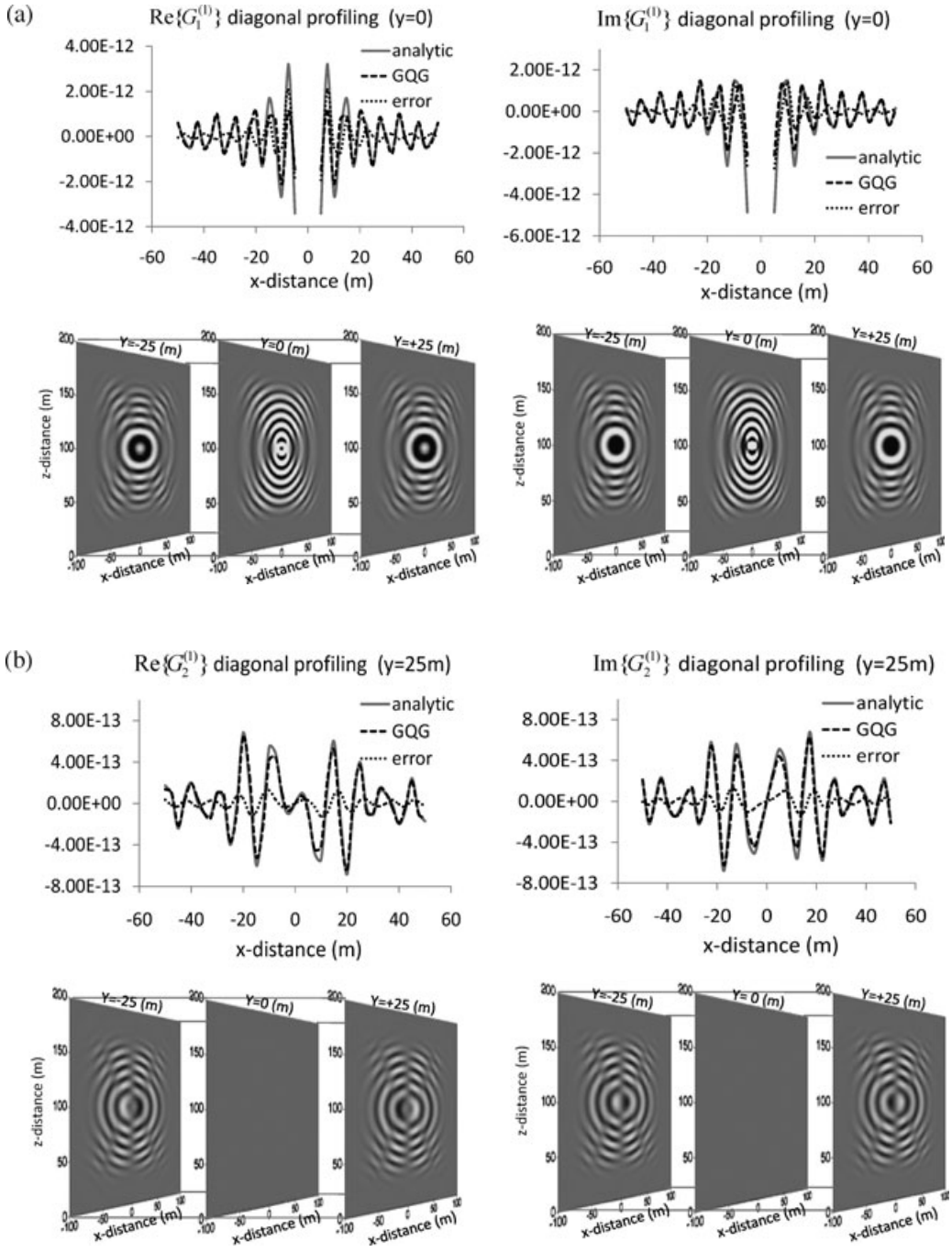

Figure 4. Six independent components of the GQG solutions for a 3-D full-space homogeneous anisotropic medium ($\rho = 1000$ kg m^{-3}, $c_{11} = c_{33} = 6.25 \times 10^9$, $c_{44} = 1.0 \times 10^9$, $c_{66} = 2.25 \times 10^9$ kg m^{-1} s^{-2}). (a) $G_1^{(1)}$-component, (b) $G_2^{(1)}$-component, (c) $G_3^{(1)}$-component, (d) $G_2^{(2)}$-component, (e) $G_3^{(2)}$-component and (f) $G_3^{(3)}$-component.

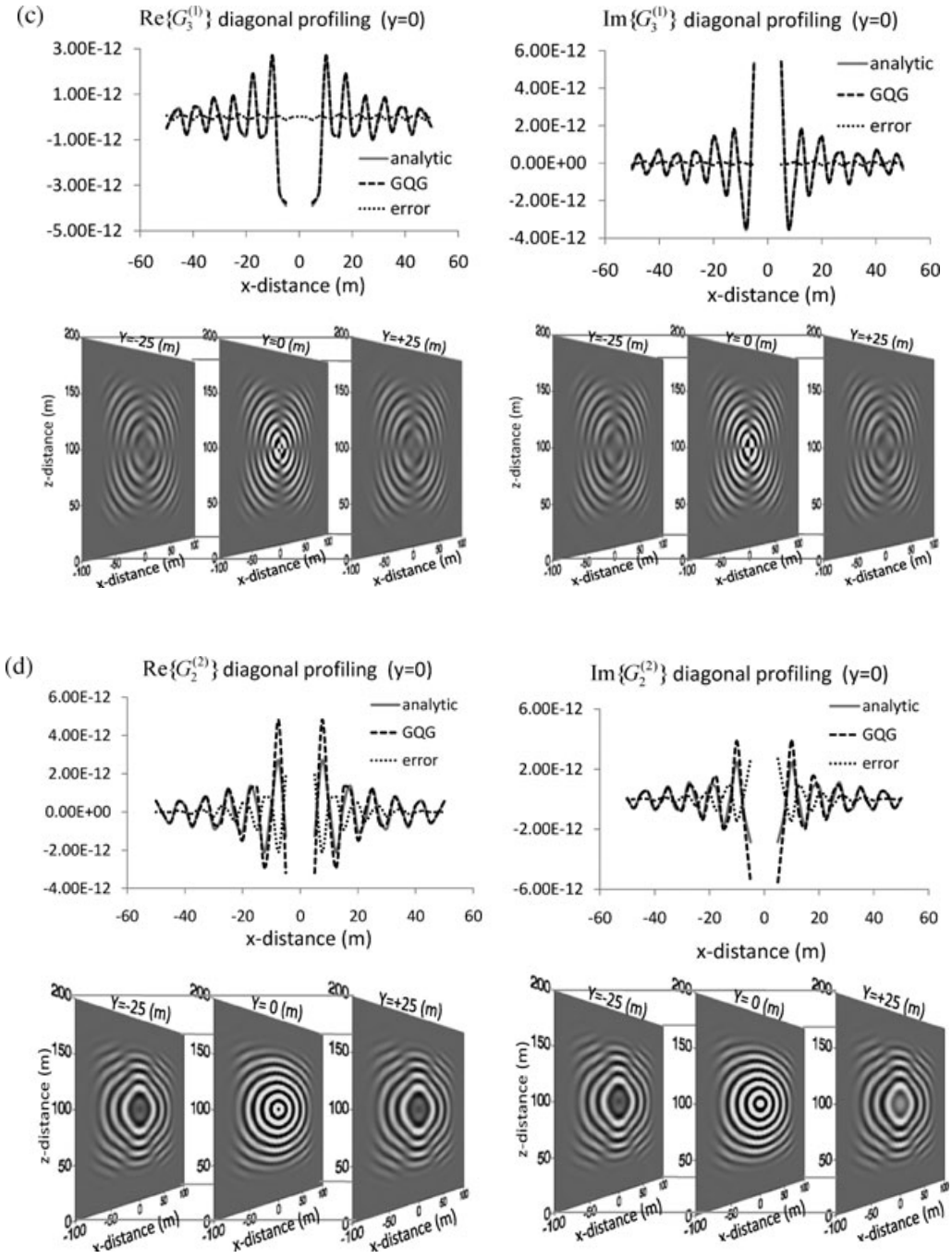

Figure 4. (*Continued.*)

for asymmetrical sparse matrices stored in a compressed full-row storage scheme; they double the computer memory in our case and are not optimal ones for the GQG approach. Therefore, we temporarily apply the sequential iterative solver BiCG (Henk 2003) to eq. (32) to obtain the numerical results. Each solution requires about 78 hr of CPU-time on an SGI Alix 3000 supercomputer, but we believe that with the continuing development of more powerful computer workstations and high performance parallel computation, the problem of the frequency-domain modelling will be eventually routinely tractable. A parallelized pre-conditioned iterative solver (Henk 2003) using the least-memory storage scheme will be available in the future, and the computational efficiency of the 3-D GQG approach will be much improved.

Figs 3 and 4 show the GQG results for the two full-space homogenous models. In each figure we give the real $\mathrm{Re}\{G_j^{(i)}\}$ and imaginary parts $\mathrm{Im}\{G_j^{(i)}\}$ of the six independent components ($G_1^{(1)}$, $G_2^{(1)}$, $G_3^{(1)}$, $G_2^{(2)}$, $G_3^{(2)}$, $G_3^{(3)}$) of the three Green's function vectors $\mathbf{G}^{(1)} = (G_1^{(1)}, G_2^{(1)}, G_3^{(1)})$, $\mathbf{G}^{(2)} = (G_1^{(2)}, G_2^{(2)}, G_3^{(2)})$ and $\mathbf{G}^{(3)} = (G_1^{(3)}, G_2^{(3)}, G_3^{(3)})$. For each component, we show three sections at $y = -25$ m, 0, $+25$ m and the profiling curves along the diagonal line in the central or off-central plane. We also compare them with the analytic solutions and give the errors (differences) along the same lines. From the diagrams, one can make the following observations: (1) whether the medium is isotropic or anisotropic, the wavefield in the margin areas (computational edges) almost disappears, which shows that the new implementation of the PML

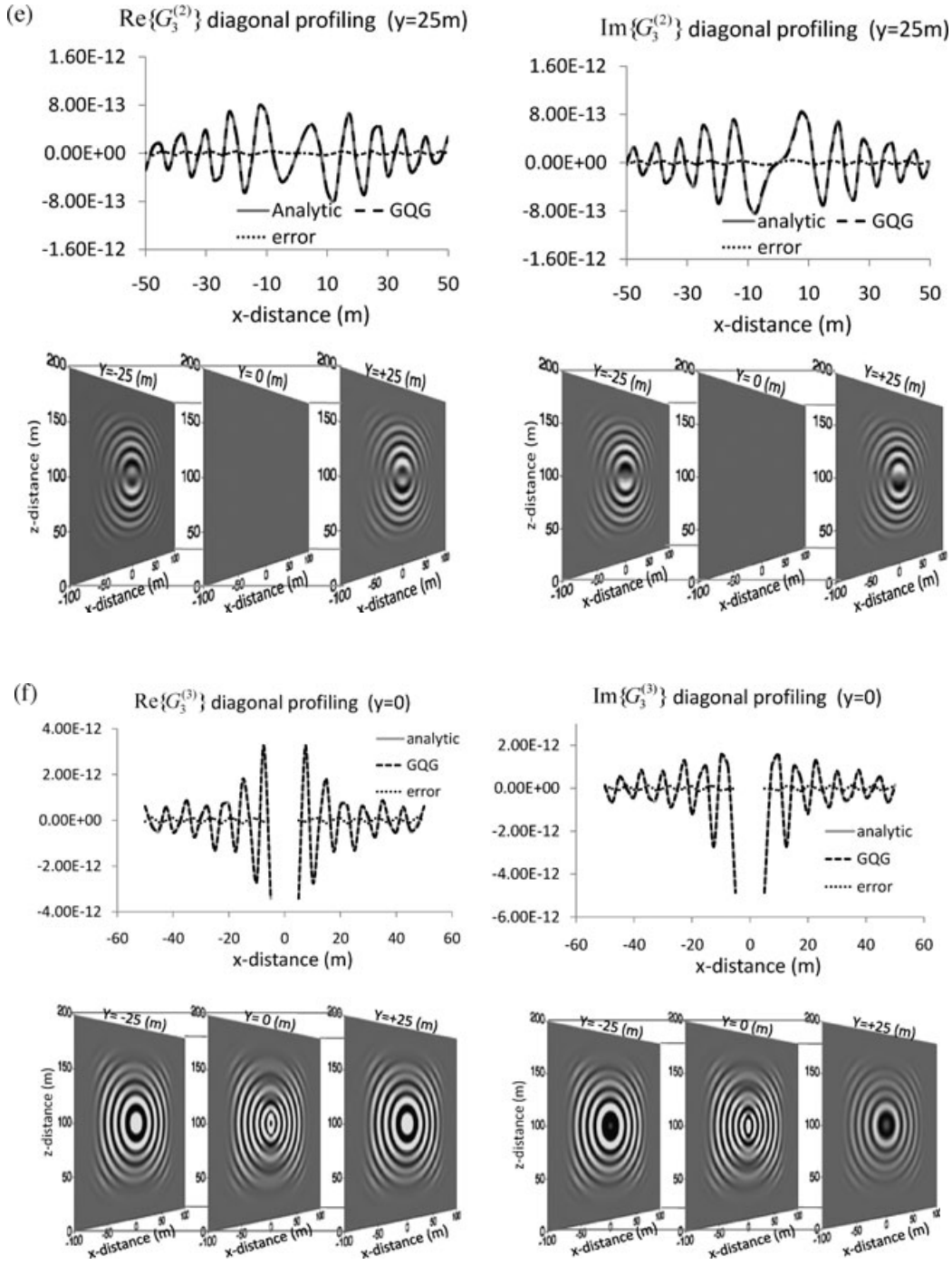

Figure 4. (*Continued.*)

defined by eq. (12) works well; (2) the diagonal curves in the central or off-central plane display a symmetric wavefield both in isotropic and anisotropic media. Furthermore, the GQG solutions match very well with the analytic solutions, except in the near-vicinity of the source at which the analytical solution becomes infinite while the GQG solutions are bounded, that is, see Figs 4(a) and (d) showing the components of $G_1^{(1)}$ and $G_2^{(2)}$, however, both are consistent with the results (see Fig. 5) obtained by 2.5-D modelling. This indicates the common disadvantage of the numerical approaches to the wavefields near the source; (3) in the isotropic medium, the wavefields reveal wave fronts of concentric circles (Figs 3a and d), or half circles (Figs 3b and e), or quarter circles (Fig. 3c), which demonstrate the difference in the Green's function vectors due to the different vibration directions of the unit source vectors; (4) in the anisotropic medium, the wavefields display wave front changes with radial direction from the point-source, that is, Figs 4(a) and (d) show that the wave fronts in the off-central plane ($y = -25$ m, $+25$ m) are no longer the concentric circles shown in Figs 3(a) and (d). Also, comparing Fig. 3(b) with Fig. 4(b), one can see the half-circle patterns in the isotropic medium are apparently distorted due to the anisotropic property. Such significant changes indicate the difference between isotropic and anisotropic media. We have compared the accuracy, run time and memory requirements for different GQ sampling

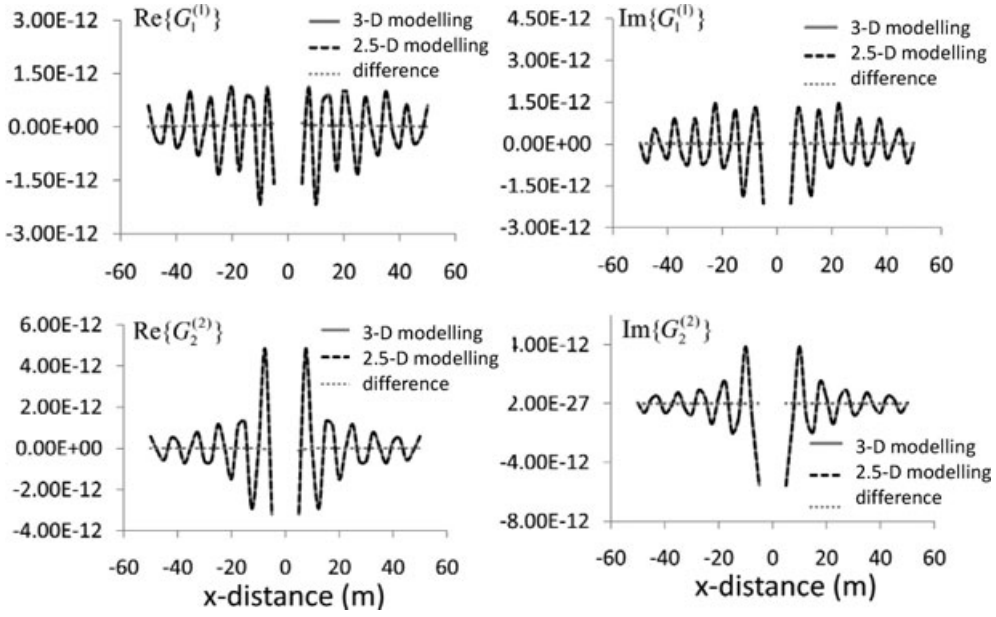

Figure 5. Comparisons of the $G_1^{(1)}$ and $G_2^{(2)}$ numerical solutions shown in Figs 4(a) and (d) with the ones obtained by 2.5-D wave modelling code.

Table 1 The rms errors and computer costs of the GQG approach for frequency-domain wavefield modelling in a 3-D full-space homogeneous anisotropic medium. The numbers are based on the SGI Altix 3000 supercomputer and a sequential BiCG-solver. Here *N*G is the Gaussian quadrature (GQ) sampling density that is defined by the number of Gaussian quadrature abscissae in the minimum wavelength.

GQ sampling density (NG)	$\mathrm{Re}\{G_1^{(1)}\}$ $\mathrm{Im}\{G_3^{(1)}\}$	$\mathrm{Re}\{G_3^{(1)}\}$ $\mathrm{Im}\{G_2^{(2)}\}$	$\mathrm{Re}\{G_2^{(2)}\}$ $\mathrm{Im}\{G_3^{(3)}\}$	$\mathrm{Re}\{G_3^{(3)}\}$	Grid & memory	CPU time (hours)
NG = 5	5.81E-13	7.31E-13	4.98E-13	8.34E-13	61 × 61 × 61	10.9
	7.86E-13	7.48E-13	5.33E-13	2.03E-12	1.4 GB	
NG = 9	3.26E-13	8.22E-14	3.79E-13	8.94E-14	121 × 121 × 121	46.5
	4.39E-13	8.24E-14	3.47E-13	9.03E-14	13 GB	
NG = 11	3.60E-13	4.19E-14	3.49E-13	3.96E-14	161 × 161 × 161	113
	3.14E13	3.55E-14	4.58E-13	3.99E-14	24 GB	

densities of NG = 5, 9 and 11 using the full space anisotropic model, for which the analytic solution is known. Results are given in Table 1. Errors are tabulated for both real and imaginary parts of four of the components of the Green's tensor. Note how errors decrease as the Gaussian order increases, but the grid size and hence the memory and CPU time increase at a much greater rate than the reduction in error.

The third model is a two-layered anisotropic medium incorporating a surface ridge (see Fig. 1). The model dimensions are 180 km × 180 km × 150 km. The model parameters are given by $\mathbf{m}_1 = \{\rho = 1000\ \mathrm{kg\,m^{-3}}, c_{11} = 6.25 \times 109, c_{13} = 4.25 \times 10^9, c_{33} = 5.25 \times 10^9, c_{44} = 1.0 \times 10^9, c_{66} = 2.25 \times 10^9\ \mathrm{kg\,m^{-1}\,s^{-2}}\}$ for the first layer and $\mathbf{m}_2 = \{\rho = 900\ \mathrm{kg\,m^{-3}}, c_{11} = c_{33} = 3.60 \times 10^9, c_{13} = 1.20 \times 10^9, c_{33} = 4.50 \times 10^9, c_{44} = 1.2 \times 10^9, c_{66} = 1.75 \times 10^9\ \mathrm{kg\,m^{-1}\,s^{-2}}\}$ for the second layer. We individually set up the three unit source vectors below the ridge at 10 km depth and whose directions coincide with the three orthogonal axes, then calculate the responses of the displacement vectors at a frequency of 0.1 Hz for the three sources. Figs 6(a)–(c) show the three sections ($y = -25$, 0, $+25$ km) of the real parts (left three columns) and imaginary parts (right three columns) of the displacement vectors (Green's function vectors) corresponding to the three unit source vectors in the 3-D volume. From the results, one can observe the following features of the frequency-domain wavefields: (1) looking at each row in Figs 6(a)–(c), one can observe that the elliptic wave fronts in the first layer (of thickness 50 km) are distorted by the reflections from the free-surface and the sub-surface, the wavelengths in the two layers are apparently different and the normal directions of the wave fronts change or refract at the contact between the two layers; (2) comparing each row in Fig. 6(a) with those in Figs 6(b) and (c), one finds that the wave front patterns are quite different for the three source vectors; this implies that the components of the displacement vectors vary with the source vibration directions; (3) the symmetric and antisymmetric wavefields are displayed in the off-central sections as the source vector is symmetric or anti-symmetric to the sections, that is, looking at the top and bottom rows in Figs 6(a) and (c), and the middle row in Fig. 6(b), one can see that the wavefields in the sections at $y = -25$ km and at $y = +25$ km are symmetric, whereas the others are all antisymmetric with respect to the central section ($y = 0$) where zero wavefields appear. This may be analytically proved. To validate the 3-D modelling results, we employed our 2.5-D frequency-domain modelling code and computed the 3-D wavefields in the same model. Fig. 7 shows the two sets of modelling results along the free-surface central line, from which one can see that they are highly consistent except for

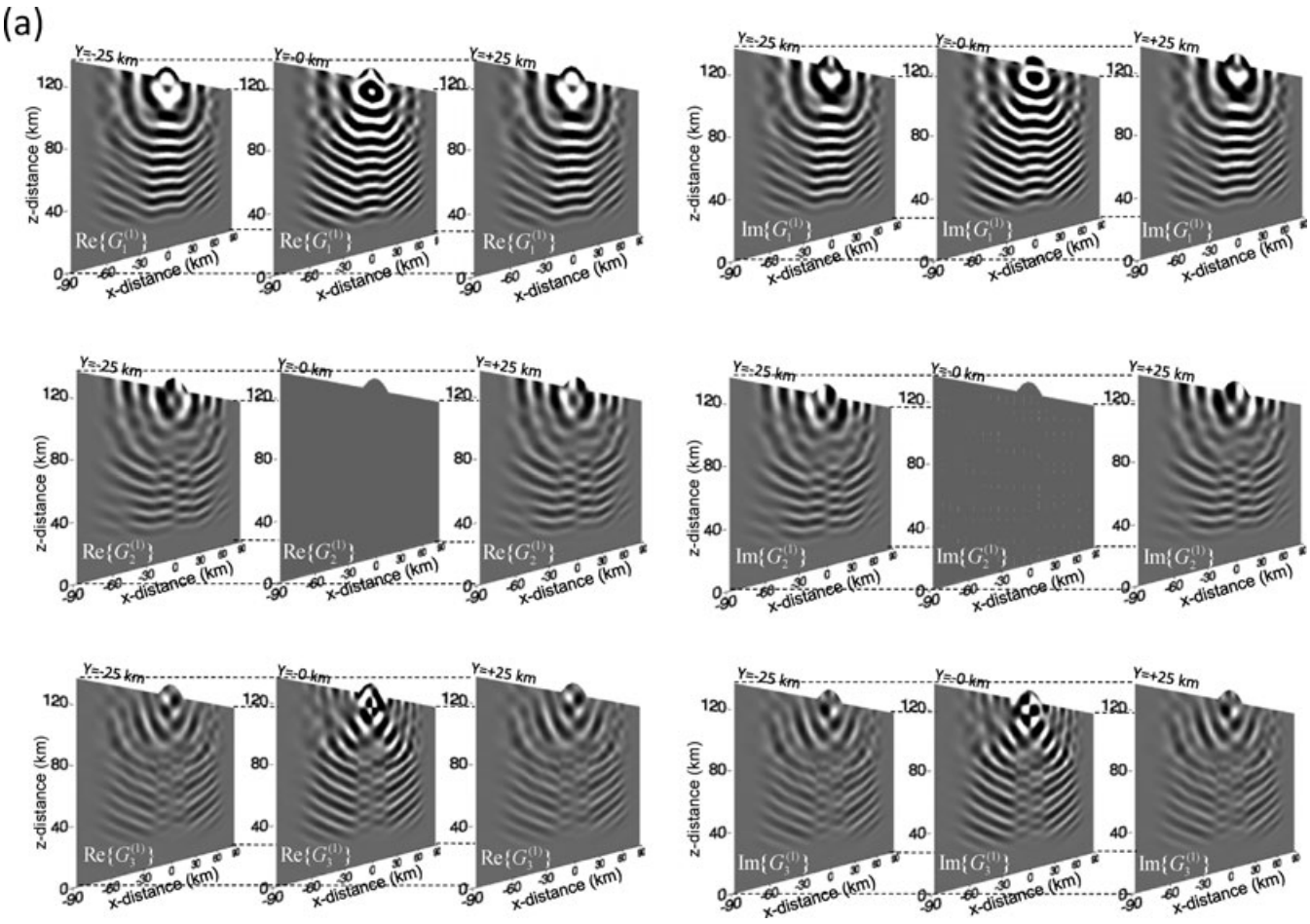

Figure 6. 3-D real and imaginary components of the wavefields at a frequency of 0.1 Hz, generated by the unit source vector acting in the (a) *x*-direction, (b) *y*-direction and (c) *z*-direction at a depth of 10 km beneath the ridge in the two-layered, anisotropic model (see Fig. 1), whose model parameters are given by $\mathbf{m}_1 = \{\rho = 1000\ \mathrm{kg\,m^{-3}}, c_{11} = 6.25 \times 10^9, c_{13} = 4.25 \times 10^9, c_{33} = 5.25 \times 10^9, c_{44} = 1.0 \times 10^9, c_{66} = 2.25 \times 10^9\ \mathrm{kg\,m^{-1}\,s^{-2}}\}$ and $\mathbf{m}_2 = \{\rho = 900\ \mathrm{kg\,m^{-3}}, c_{11} = c_{33} = 3.60 \times 10^9, c_{13} = 1.20 \times 10^9, c_{33} = 4.50 \times 10^9, c_{44} = 1.2 \times 10^9, c_{66} = 1.75 \times 10^9\ \mathrm{kg\,m^{-1}\,s^{-2}}\}$.

near the source (middle of the line). This comparison demonstrates that both methods have the capability to simulate the frequency-domain wavefields for realistic applications.

CONCLUSIONS

We have presented a frequency-domain version of the SEM, called the GQG approach, for 3-D frequency-domain seismic wave modelling in a general anisotropic medium, which may incorporate a free-surface topography and irregular sub-surface interfaces. The two most innovative and attractive features of the GQG approach are simplification of the model discretization and incorporation of a new PML implementation with the numerical method. Using an appropriate density of the Gaussian quadrature points enables us to easily sample the model parameters in terms of the model geometries, including a variable free-surface topography and sub-surface discontinuities, and obtain satisfactory results for the frequency-domain wavefields. The new PML implementation is simple, general, effective and extendable to any class of anisotropic medium. The GQG approach may be employed as the forward modelling part that yields the synthetic spectral data at a few frequencies that are required in generalized diffraction tomography and in frequency-domain full-waveform inversion. It can also be used to compute the sensitivity kernels (Fréchet derivatives) at the requisite or dominant frequencies in heterogeneous, anisotropic media for given configurations of source-geophone pairs (Zhou & Greenhalgh 2009). In addition, it may be applied to simulate the site-effects of ground motion at various frequencies.

The accuracy of the GQG approach is controlled by the number of Gaussian quadrature points in the minimum wavelength, or the so-called sampling density of the Gaussian quadrature abscissae. The optimal sampling density should be the one that offers a point-gridded model that enables high definition of the geological characteristics and high accuracy of the variational integral and spatial differentiation. Our experiments show that satisfactory results may be obtained by using sampling densities larger than five points per minimum wavelength.

Efficiency of the GQG approach mainly depends on the linear-system solver of a large dimensional, sparse and symmetric complex matrix. The compressed half-row storage scheme is the one requiring the least computer memory, but with such an optimal storage scheme,

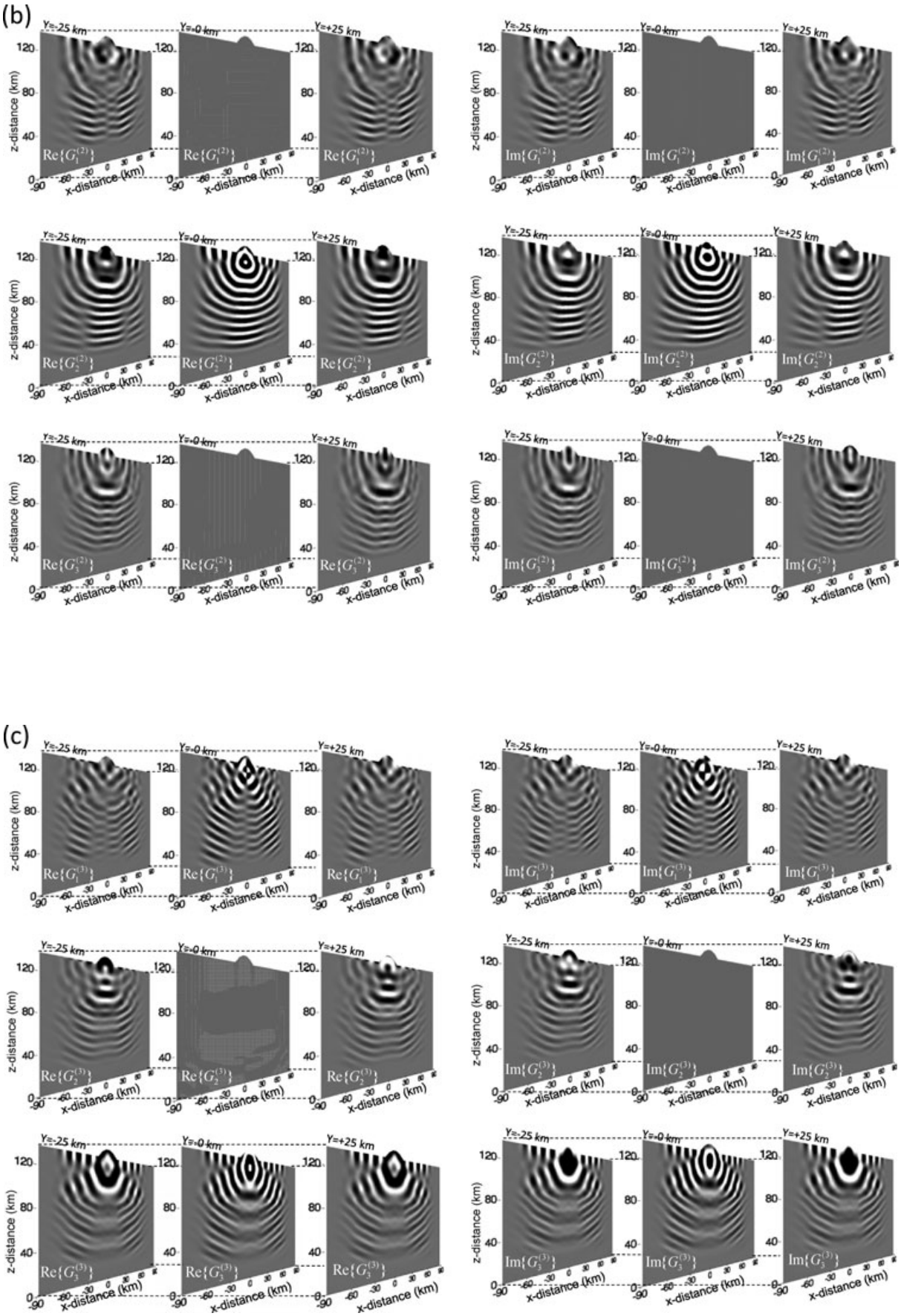

Figure 6. (*Continued.*)

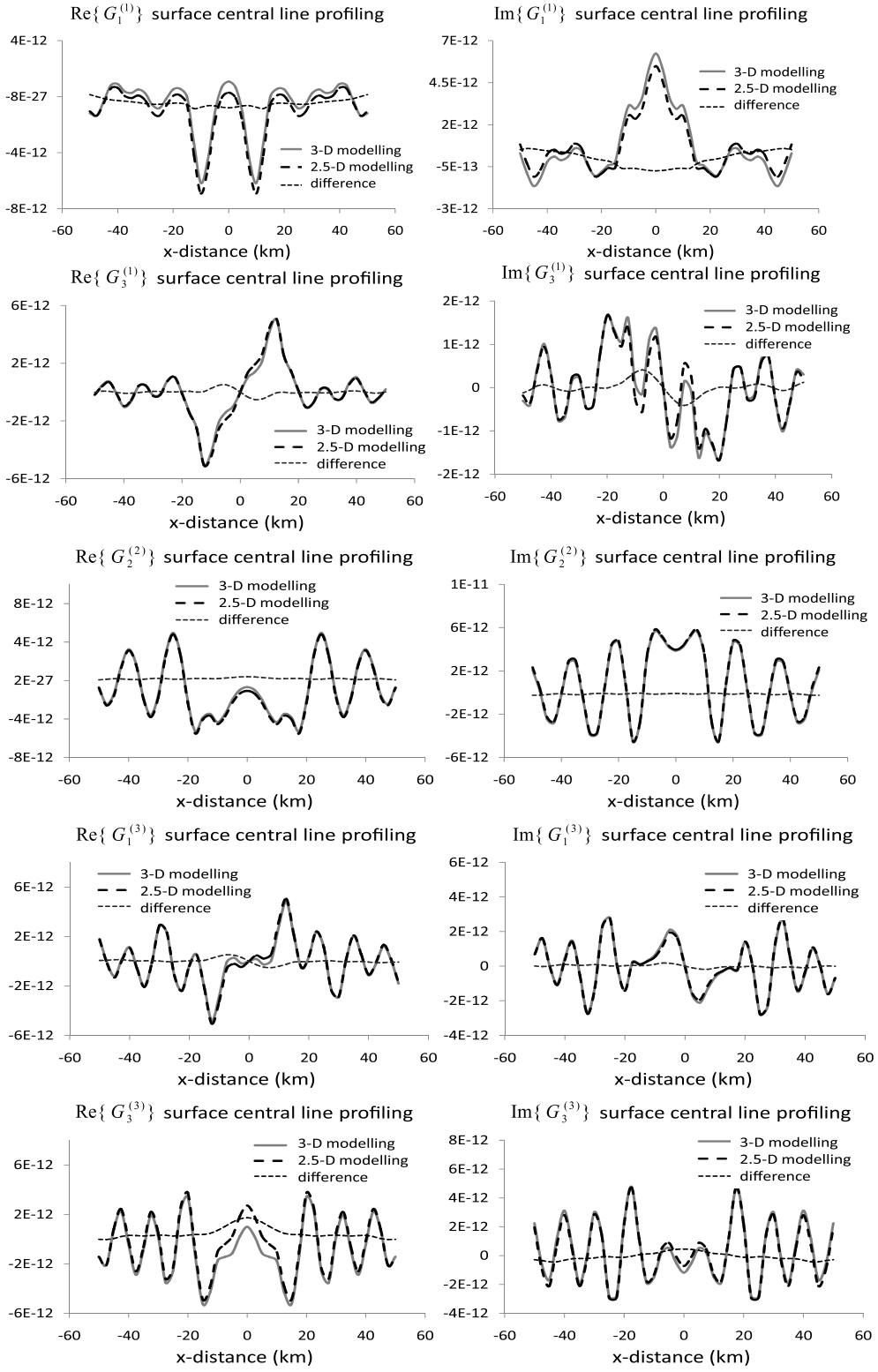

Figure 7. Five independent tensor components of the 3-D frequency-domain wavefields along the free-surface central line, which are obtained by 3-D and 2.5-D modelling methods for the two-layered anisotropic model having a ridge on its free-surface, shown in Fig. 1.

the sequential, iterative Krylov solvers are still very expensive in computer time due to their slow convergence. Therefore, it is crucial to improve the computational efficiency of the GQG approach by developing a parallelized iterative preconditioned Krylov solver (Henk 2003) with such optimal storage scheme in the future.

ACKNOWLEDGMENTS

This work was supported by the Australian Research Council and the Swiss National Science Foundation. The authors thank Dr Simon Brennan of the Helpdesk at eResearch SA who provided assistance in using the advanced super-computing facilities for this project. The authors also greatly appreciate the insightful criticisms and constructive suggestions of the Associate Editor and two reviewers, which have improved the paper considerably.

REFERENCES

Aki, K. & Richards, P.G., 1980. *Quantitative Seismology: Theory and Methods,* Vol. 1, W. H. Freeman and Company, New York.

Ali, H.B.H., Operto, S. & Virieux, J., 2008. Velocity model building by 3D frequency-domain full-waveform inversion of wide-aperture seismic data, *Geophysics,* **73,** VE101–VE117.

Bailey, D.H., Jeyabalan, K. & Li, X.S., 2005. A comparison of three high-precision quadrature schemes, *Exp. Math.,* **14,** 3, 317–329.

Basabe, J., Sen, M.K. & Wheeler, M.F., 2008. The interior penalty discontinuous Galerkin method for elastic wave propagation: grid dispersion, *Geophys. J. Int.,* **175,** 83–93.

Becker, E.B., Carey, G.F. & Oden, J.T., 1983. *Finite Elements, A Second Course,* Vol. 2, Prentice-Hall, Inc., Englewood Cliffs, New Jersey.

Berenger, J.P., 1994. A perfectly matched layer for the absorbing of electromagnetic waves, *J. comput. Phys.,* **114,** 185–200.

Carcione, J.M., 1994. The wave equation in generalized coordinates, *Geophysics,* **59,** 1911–1919.

Carcione, J.M., 2001. *Wave Fields in Real Media: Wave Propagation in Anisotropic, Anelastic and Porous Media,* Pergamon, Amsterdam, The Netherlands.

Crampin, S., 1981. A review of wave motion in anisotropic and cracked elastic-media, *Wave Motion,* **3,** 343–391.

Crandall, R.E., 1996. Topics in Advanced Scientific Computations, Springer-Verlag, Berlin.

Dumbser, M., Käser, M. & Eleuterio, F.T., 2007. An arbitrary high-order Discontinuous Galerkin method for elastic waves on unstructured mesh—V. Local time stepping and p-adaptivity, *Geophys. J. Int.,* **171,** 695–717.

Emanuele, C., Stupazzini, M., Lee, S.J., Komatitsch, D., Piersanti, A. & Tromp J., 2007. CUBIT and Seismic wave propagation based upon the spectral-element method: an advanced unstructured mesher for complex 3D geological media, in *Proceedings of the 16th International Meshing Roundtable,* edsBrewer, M.L. & Marcum, D., Springer, Berlin, Heidelberg.

Faccioli, E., Maggio, F., Paolucci, R. & Quarteroni, A., 1997. 2D and 3D elastic wave propagation by a pseudo-spectral domain decomposition method, *J. Seismol.,* **1,** 237–251.

Festa, G. & Vilotte, J., 2005. The Newmark scheme as velocity-stress time-staggering: an efficient PML implementation for spectral element simulations of elastrodynamics, *Geophys. J. Int.,* **161,** 789–812.

Fichtner, A., Kennett, B.L.N., Igel, H. & Bunge, H.P., 2009a. Full waveform tomography for radially anisotropic structure: new insights into present and past states of the Australasian upper mantle, *Earth planet. Sci. Lett.,* **290,** 270–280.

Fichtner, A., Igel, H., Bunge, H.P. & Kennett, B.L.N., 2009b. Simulation and inversion of seismic wave propagation on continental scales based on a spectral-element method, *J. Numer. Anal.: Ind. Appl. Math.,* **4**(1–2), 11–22.

Filippone, S. & Colajanni, M., 2000. PSBLAS: a library for parallel linear algebra computation on sparse matrices, *ACM Trans. Math. Softw.,* **26,** No. 4, 527–550.

Fujii, A., Suda, R., Nishida, A. & Oyanagi, Y., 2007. Evaluation of synchronous Iterative Method for Sparse Matrix Solver, in *Proceedings of the Second International Workshop on Automatic Performance Tuning,* 43–51.

Furumura, T., Kennett, B.L.N. & Furumura, M., 1998. Seismic wavefield calculation for laterally heterogeneous whole earth models using the pseudo-spectral method, *Geophys. J. Int.,* **135,** 845–860.

Gelius, L.J., 1995. Generalized acoustic diffraction tomography, *Geophys. Prospect.,* **43,** 3–29.

Greenhalgh, S.A. & Zhou, B., 2003. Surface seismic imaging by multi-frequency amplitude inversion, *Explor. Geophys.,* **34,** 217–224.

Henk, A., 2003. *Iterative Krylov Methods for Large Linear Systems,* Cambridge University Press, United Kingdom.

Hestholm, S. & Ruud, B., 1998. 3-D finite-difference elastic wave modelling including surface topography, *Geophysics,* **63,** 613–622.

Igel, H., 1999. Wave propagation in a three-dimensional spherical section by the Chebyshev spectral method, *Geophys. J. Int.,* **136,** 559–566.

Kelley, K.R. & Marfurt, K.J., 1990. *Numerical Solutions of Acoustic and Elastic Wave Equations—Finite Difference and Finite Element Algorithms,* Society of Exploration Geophysics, USA.

Kerry, K. & Weiss, C., 2006. Adaptive finite element modelling using unstructured grids: the 2D magnetotelluric example, *Geophysics,* **71,** G291–G294.

Komatitsch, D. & Tromp, J., 2002. Spectral-element simulation of global seismic wave propagation I Validation, *Geophys. J. Int.,* **149,** 390–412.

Komatitsch, D. & Tromp, J., 2003. A perfect matched layer absorbing boundary condition for the second-order seismic wave equation, *Geophys. J. Int.,* **154,** 146–153.

Komatitsch, D. & Vilotte, J., 1998. The spectral element method: an efficient tool to simulate the seismic response of 2D and 3D geological structures, *Bull. seism. Soc. Am.,* **88,** 368–392.

Komatitsch, D., Coutel, F. & Mora, P., 1996. Tensorial formulation of the wave equation for modelling curved interfaces, *Geophys. J. Int.,* **127,** 156–168.

Kosloff, D., Kessler, D., Filho, A., Tessmer, E., Behle, A. & Strhilevitz, R., 1990. Solution of the equation of dynamic elasticity by a Chebyshev spectral method, *Geophysics,* **55,** 734–748.

Li, X.S. & Demmel, J.W., 2003. SuperLU_DIST: a scalable distributed-memory sparse direct solver for unsymmetric linear systems, *ACM Trans. Math. Softw.* **29,** 110–140.

Maurer, H., Greenhalgh, S.A. & Latzel, S., 2009, Frequency and spatial sampling strategies for crosshole seismic waveform inversion experiments, *Geophysics,* **74,** WCC79–WCC89.

Nihei, K. & Xiaoye, L., 2007. Frequency response modelling of seismic waves using finite difference time domain with phase sensitive detection (TD-PSD), *Geophys. J. Int.,* **169,** 1069–1078.

Phillip, J. & Rabinowitz, P., 1984. *Methods of Numerical Integration,* Academic Press, New York.

Pratt, R.G., 1999. Seismic waveform inversion in the frequency-domain, Part I: theory and verification in a physical scale model, *Geophysics,* **64,** 902–914.

Rücker, C., Gunther, T. & Spitzer, K., 2006. Three-dimensional modelling and inversion of DC resistivity data incorporating topography, I: modelling, *Geophys. J. Int.,* **166,** 495–505.

Schenk, O. & Gärtner, K., 2004. Solving unsymmetric sparse systems of linear equations with PARDISO. *J. Future Gener. Comput. Syst.* **20,** 475–487.

Shewchuk, J.R., 2002. Delaunay refinement algorithms for triangular mesh generation, *Comput. Geom.—Theory Appl.,* **22,** 21–74.

Sinclair, C.E., 2009. Elastic wave modelling in anisotropic media using the spectral-element method, *PhD thesis*, Adelaide University.

Sinclair, C.E., Greenhalgh, S.A. & Zhou, B., 2007. 2.5D modelling of elastic waves in transversely isotropic media using the spectral element method, *Explor. Geophys.,* **38,** 225–234.

Sirgue, L., Stefani, J.T. & Albertin, U., 2008. 3D frequency-domain inversion using time-domain finite difference methods, in *70th Conference and Exhibition, EAGE, Extended Abstract,* Rome, F022.

Takahasi, H. & Mori, M., 1974. Double exponential formulas for numerical integration, *Publications of RIMS, Kyoto University*, **9,** 721–741.

Tape, C., Liu, Q.Y. Maggi, A. & Tromp, J., 2009. Adjoint tomography of the Southern California crust, *Science,* **325,** 988–992.

Tessmer, E., 1995. 3-D seismic modelling of general material anisotropy in the presence of the free surface by a Chebyshev spectral method, *Geophys. J. Int.,* **121,** 557–575.

Thomsen, L., 1986. Weak elastic anisotropy, *Geophysics,* **51,** 1954–1966.

Trefethen, L.N., 2000. *Spectral Methods in MATLAB,* SIAM, Philadelphia.

Vavrycuk, V., 2007. Asymptotic Green's function in homogeneous anisotropic viscoelastic media, *Proc. R. Soc. A,* **463,** 2689–2707.

Wu, R.-S. & Toksoz, M.N., 1987. Diffraction tomography and multisource holography applied to seismic imaging, *Geophysics,* **52,** 11–25.

Zhou, B. & Greenhalgh, S.A., 2003. Crosshole seismic inversion with normalized full-waveform amplitude data, *Geophysics,* **68,** 1320–1330.

Zhou, B. & Greenhalgh, S.A., 2009. On the computation of the Fréchet derivatives for seismic waveform inversion in 3D general anisotropic, heterogeneous media. *Geophysics,* **74,** WB153–WB163.

Zhou, B., Greenhalgh, M. & Greenhalgh, S.A., 2009. 2.5-D/3-D resistivity modelling in anisotropic media using Gaussian quadrature grids, *Geophys. J. Int.,* **176,** 63–80.

APPENDIX: DIFFERENTIAL MATRICES

$$\mathbf{A}_1^p = \tilde{c}_{1111}\mathbf{D}_x^T\mathbf{D}_x + 0.5(\tilde{c}_{1112}+\tilde{c}_{2111})(\mathbf{D}_x^T\mathbf{D}_y + \mathbf{D}_y^T\mathbf{D}_x) + 0.5(\tilde{c}_{1113}+\tilde{c}_{3111})(\mathbf{D}_x^T\mathbf{D}_z + \mathbf{D}_z^T\mathbf{D}_x) + \tilde{c}_{2112}\mathbf{D}_y^T\mathbf{D}_y + 0.5(\tilde{c}_{3112}+\tilde{c}_{2113})(\mathbf{D}_y^T\mathbf{D}_z + \mathbf{D}_z^T\mathbf{D}_y) + \tilde{c}_{3113}\mathbf{D}_z^T\mathbf{D}_z]. \quad \text{(A1)}$$

$$\mathbf{A}_2^p = \tilde{c}_{1221}\mathbf{D}_x^T\mathbf{D}_x + 0.5(\tilde{c}_{1222}+\tilde{c}_{2221})(\mathbf{D}_x^T\mathbf{D}_y + \mathbf{D}_y^T\mathbf{D}_x) + 0.5(\tilde{c}_{1223}+\tilde{c}_{3221})(\mathbf{D}_x^T\mathbf{D}_z + \mathbf{D}_z^T\mathbf{D}_x) + \tilde{c}_{2222}\mathbf{D}_y^T\mathbf{D}_y + 0.5(\tilde{c}_{2223}+\tilde{c}_{3222})(\mathbf{D}_y^T\mathbf{D}_z + \mathbf{D}_z^T\mathbf{D}_y) + \tilde{c}_{3223}\mathbf{D}_z^T\mathbf{D}_z. \quad \text{(A2)}$$

$$\mathbf{A}_3^p = \tilde{c}_{1331}\mathbf{D}_x^T\mathbf{D}_x + 0.5(\tilde{c}_{1332}+\tilde{c}_{2331})(\mathbf{D}_x^T\mathbf{D}_y + \mathbf{D}_y^T\mathbf{D}_x) + 0.5(\tilde{c}_{1333}+\tilde{c}_{3331})(\mathbf{D}_x^T\mathbf{D}_z + \mathbf{D}_z^T\mathbf{D}_x) + \tilde{c}_{2332}\mathbf{D}_y^T\mathbf{D}_y + 0.5(\tilde{c}_{2333}+\tilde{c}_{3332})(\mathbf{D}_y^T\mathbf{D}_z + \mathbf{D}_z^T\mathbf{D}_y) + \tilde{c}_{3333}\mathbf{D}_z^T\mathbf{D}_z. \quad \text{(A3)}$$

$$\mathbf{A}_4^p = (\tilde{c}_{1121}+\tilde{c}_{1211})\mathbf{D}_x^T\mathbf{D}_x + 0.5(\tilde{c}_{1122}+\tilde{c}_{2211})(\mathbf{D}_x^T\mathbf{D}_y + \mathbf{D}_y^T\mathbf{D}_x) + 0.5(\tilde{c}_{1123}+\tilde{c}_{3211})\cdot (\mathbf{D}_x^T\mathbf{D}_z + \mathbf{D}_z^T\mathbf{D}_x) + 0.5(\tilde{c}_{1212}+\tilde{c}_{2121})(\mathbf{D}_y^T\mathbf{D}_x + \mathbf{D}_x^T\mathbf{D}_y) + (\tilde{c}_{2122}+\tilde{c}_{2212})\mathbf{D}_y^T\mathbf{D}_y + 0.5(\tilde{c}_{2123}+\tilde{c}_{3212})(\mathbf{D}_y^T\mathbf{D}_z + \mathbf{D}_z^T\mathbf{D}_y) + 0.5(\tilde{c}_{1213}+\tilde{c}_{3121})(\mathbf{D}_z^T\mathbf{D}_x + \mathbf{D}_x^T\mathbf{D}_z) + 0.5 \cdot 0.5(\tilde{c}_{2213}+\tilde{c}_{3122})(\mathbf{D}_z^T\mathbf{D}_y + \mathbf{D}_y^T\mathbf{D}_z) + (\tilde{c}_{3123}+\tilde{c}_{3213})\mathbf{D}_z^T\mathbf{D}_z. \quad \text{(A4)}$$

$$\mathbf{A}_5^p = (\tilde{c}_{1131}+\tilde{c}_{1311})\mathbf{D}_x^T\mathbf{D}_x + 0.5(\tilde{c}_{1132}+\tilde{c}_{2311})(\mathbf{D}_x^T\mathbf{D}_y + \mathbf{D}_y^T\mathbf{D}_x) + 0.5(\tilde{c}_{1133}+\tilde{c}_{3311})\cdot (\mathbf{D}_x^T\mathbf{D}_z + \mathbf{D}_z^T\mathbf{D}_x) + 0.5(\tilde{c}_{1312}+\tilde{c}_{2131})(\mathbf{D}_y^T\mathbf{D}_x + \mathbf{D}_x^T\mathbf{D}_y) + (\tilde{c}_{2132}+\tilde{c}_{2312})\mathbf{D}_y^T\mathbf{D}_y + 0.5(\tilde{c}_{2133}+\tilde{c}_{3312})(\mathbf{D}_y^T\mathbf{D}_z + \mathbf{D}_z^T\mathbf{D}_y) + 0.5(\tilde{c}_{1313}+\tilde{c}_{3131})(\mathbf{D}_z^T\mathbf{D}_x + \mathbf{D}_x^T\mathbf{D}_z) + 0.5\cdot (\tilde{c}_{2313}+\tilde{c}_{3132})(\mathbf{D}_z^T\mathbf{D}_y + \mathbf{D}_y^T\mathbf{D}_z) + (\tilde{c}_{3133}+\tilde{c}_{3313})\mathbf{D}_z^T\mathbf{D}_z. \quad \text{(A5)}$$

$$\mathbf{A}_6^p = (\tilde{c}_{1321}+\tilde{c}_{1231})\mathbf{D}_x^T\mathbf{D}_x + 0.5(\tilde{c}_{1232}+\tilde{c}_{2321})(\mathbf{D}_x^T\mathbf{D}_y + \mathbf{D}_y^T\mathbf{D}_x) + 0.5(\tilde{c}_{1233}+\tilde{c}_{3321})\cdot (\mathbf{D}_x^T\mathbf{D}_z + \mathbf{D}_z^T\mathbf{D}_x) + 0.5(\tilde{c}_{1322}+\tilde{c}_{2231})(\mathbf{D}_y^T\mathbf{D}_x + \mathbf{D}_x^T\mathbf{D}_y) + (\tilde{c}_{2232}+\tilde{c}_{2322})\mathbf{D}_y^T\mathbf{D}_y + 0.5(\tilde{c}_{2233}+\tilde{c}_{3322})(\mathbf{D}_y^T\mathbf{D}_z + \mathbf{D}_z^T\mathbf{D}_y) + 0.5(\tilde{c}_{1323}+\tilde{c}_{3231})(\mathbf{D}_z^T\mathbf{D}_x + \mathbf{D}_x^T\mathbf{D}_z) + 0.5\cdot (\tilde{c}_{2323}+\tilde{c}_{3232})(\mathbf{D}_z^T\mathbf{D}_y + \mathbf{D}_y^T\mathbf{D}_z) + (\tilde{c}_{3233}+\tilde{c}_{3323})\mathbf{D}_z^T\mathbf{D}_z. \quad \text{(A6)}$$